Introducing the Flexon - a New Chiral Polarization State in Ferroelectrics

Anna N. Morozovska [1*], Riccardo Hertel[2†], Salia Cherifi-Hertel[2], Victor Yu. Reshetnyak[3],
Eugene A. Eliseev[4], and Dean R. Evans[5‡]

[1] Institute of Physics, National Academy of Sciences of Ukraine,
46, pr. Nauky, 03028 Kyiv, Ukraine
[2] Université de Strasbourg, CNRS, Institut de Physique et Chimie des Matériaux de Strasbourg,
UMR 7504, 67000 Strasbourg, France
[3] Taras Shevchenko National University of Kyiv,
Volodymyrska Street 64, Kyiv, 01601, Ukraine
[4] Institute for Problems of Materials Science, National Academy of Sciences of Ukraine,
Krjijanovskogo 3, 03142 Kyiv, Ukraine
[5] Air Force Research Laboratory, Materials and Manufacturing Directorate,
Wright-Patterson Air Force Base, Ohio, 45433, USA

---

[*] Corresponding author 1: anna.n.morozovska@gmail.com

[†] Corresponding author 2: riccardo.hertel@ipcms.unistra.fr

[‡] Corresponding author 4: dean.evans@afresearchlab.com

Abstract

Using the Landau-Ginzburg-Devonshire phenomenological approach along with electrostatic equations and elasticity theory, we perform finite element modeling of the electric polarization, electric field, and elastic stresses and strains in a core-shell nanoparticle, where the ferroelectric core has a shape of prolate cylinder. The nanoparticle is placed is a very soft elastic medium. We impose an electrical open-circuit conditions at the cylinder ends to make the vortex-type polarization energetically favorable. Calculations, performed for the sharp and rounded ends of a cylindrical $BaTiO_3$ core, reveal that the distribution of the polarization components depends critically on the curvature radius of the ends and is highly sensitive to the values of polarization gradient coefficients.

Calculations reveal the quadrupolar-type diffuse domain structure consisting of two oppositely oriented diffuse axial domains located near the cylinder ends, which are separated by a region with a zero-axial polarization; we have termed this "**flexon**" to underline the flexoelectric nature of its axial polarization. Analytical calculations and FEM results have proven that a change of the flexoelectric coefficient sign leads to a reorientation of the flexon axial polarization; as well as an anisotropy of the flexoelectric coupling critically influences the flexon formation and related domain morphology. The flexon polarization forms a drop-shaped region near the ends of the cylinder, with a distinct chiral structure that is determined by the sign of the flexoelectric coupling constant F_{ij}. Its rounded shape, combined with its distinct chiral properties and the localization nature near the surface are reminiscent of a those of Chiral Bobber structures in magnetism [Rybakov et al., Phys. Rev.Lett.115, 117201 (2015)]. In the azimuthal plane, the flexon displays the polarization state of a meron. We show that this new type of chiral polarization structure is stabilized by an anisotropic flexoelectric coupling. It is important to note that the Lifshitz invariant describing the flexoelectric effect, which couples the electric polarization and elastic strain gradients, plays a determining role in the stabilization of these chiral states [Bogdanov, JETP Lett. 68, 137 (1998)]. It thereby provides an energetic interaction that, similar to the recently predicted ferroelectric Dyzaloshinskii-Moryia interaction [Erb&Hlinka PRB 102, 024110 (2020), Zhao et al, Nat. Mater. **20**, 341 (2021)], can lead to the formation of chiral polarization states, and, by extension, ferroelectric skyrmions.

We predict that the flexon-type polarization distribution exists in the temperature range $260\text{ K} < T < 360\text{ K}$. The relatively wide temperature range (about 100 K) gives us the hope that the flexons can be observed experimentally. However, the analysis of the hysteresis loops leads to the conclusion that flexons and other domain configurations cannot be resolved from macroscopic measurements of the average polarization in a homogeneous electric field. Flexons can be observed by local methods using a strong gradient of an electric field, such as scanning piezoelectric response force microscopy, which give us the information about the local distribution of polarization with nanoscale resolution. Such chiral nanostructures could also be detected by means of resonant soft X-ray dichroism.

I. INTRODUCTION

Research on ferroelectric materials has received growing interest over the past years, driven in part by the potential of these material systems for low-power technological applications in a broad spectrum of domains [1, 2], ranging from high-density data storage to optical nano-devices. A central aspect of this field of research is the formation of ferroelectric domain structures [3], and more generally the micro- and nanoscale structure of the polarization field [4]. Although the foundations for the theoretical description of these material systems have been established decades ago [5], understanding the complex physical properties of ferroelectrics remains a challenge for fundamental research. Recent progress in this field, achieved to a large extent through advanced imaging techniques [6] and by employing modern numerical simulations [7], includes the discovery of highly complex polarization structures, such as flux closure [8, 9, 10, 11] and bubble domains [12], meandering [13, 14] and/or labyrinthine [15, 16] structures, non-Ising type chiral domain walls [17], polarization vortices [18, 19, 20], or polar skyrmions [21, 22]. The latter belong to a particular category of ferroic structures which are characterized by the spontaneous formation of helicoidal patterns. The mechanism that underpins the formation of skyrmion structures in ferroelectrics is not fully understood. A possible explanation is that these types of structures are stabilized by a Dyzaloshinskii-Moryia Interaction (**DMI**) type energy term. An antisymmetric coupling term of this type, previously known to exist in certain categories of ferromagnets [23, 24], has recently been predicted also for ferroelectric materials [25].

Traditionally, research on ferroelectrics is centered on the study of bulk material and thin films [9-14], but recently ferroelectric nanoparticles have also attracted increasing interest [15, 26]. The transition from bulk to nanostructured ferroelectrics is comparable to the development that was made in the past decades in the neighboring scientific community of ferromagnets, where it was found that the particle shape and size can have a decisive impact on their physical properties [27]. In ferroelectric thin films and nanoparticles, the polarization structure is strongly affected by electrostatic (depolarizing) fields [28, 29], as well as by strain and strain gradients [30, 31, 32, 33, 34] via the flexoelectric effect [35, 36, 37].

The thermodynamic description of the flexoelectric effect is given by the Lifshitz invariant in the free energy expansion [36]. It is known that, in magnetic materials, the occurrence of similar Lifshitz invariants converts directly into an antisymmetric coupling known as the DMI [38, 39], which favors the formation of helicoidal structures with a specific chirality. The existence of a ferroelectric counterpart of the DMI was recently predicted by first-principles simulations [25]. Similarly, in the context of Lifshitz invariants, the ferroelectric analogue of the

DMI was discussed by Strukov and Levanyuk [40], and more recently by Erb and Hlinka [41] who argued that a ferroelectric DMI can exist which could stabilize polar skyrmion structures. While the ferroelectric DMI could be at the origin of such structures, Erb and Hlinka showed that only very few and rather exotic material systems possess symmetry properties that are compatible with such an interaction. In addition to the remarkable similarity in the mathematical form of flexoelectric Lifshitz invariant and DMI, the flexoelectric term appears to have a similar impact as the DMI in terms of the formation of chiral structures.

By means of the finite element modeling (**FEM**) based on the Landau-Ginzburg-Devonshire (**LGD**) theory, we show that an anisotropic flexoelectric effect can give rise to a new type of polarization states with distinct chiral properties, which we have termed a “**flexon**”. In particular, we observe the formation of particle-like drop shaped polarization structures at opposite ends of ferroelectric nanocylinders. These polarization states possess homochiral properties which are not induced by a DMI term. This finding suggests that the recently discussed DMI in ferroelectrics is not the only possible mechanism for the formation of homochiral polarization states, and that anisotropic flexoelectric effects offer an alternative pathway to stabilize such structures in ferroelectric nanostructures. We discuss common aspects of the DMI and the flexoelectric effect, which are both derived from Lifshitz invariants in the framework of the Landau theory of second-order phase transitions.

II. CONSIDERED PROBLEM AND SIMULATION DETAILS

A. Considered Problem and Material Parameters

Using a LGD phenomenological approach along with electrostatic equations and elasticity theory, we model the polarization, the internal electric field, and the elastic stresses and strains in a core-shell nanoparticle using FEM, where the ferroelectric core is made of $BaTiO_3$ and has a cylindrical shape. The aspect ratio of the nanocylinder radius R to its length h is significantly higher than unity. The z-axis is parallel to the cylinder axis (see **Fig. 1**). The core-shell nanoparticle is placed is a very soft elastic medium (e.g., liquid).

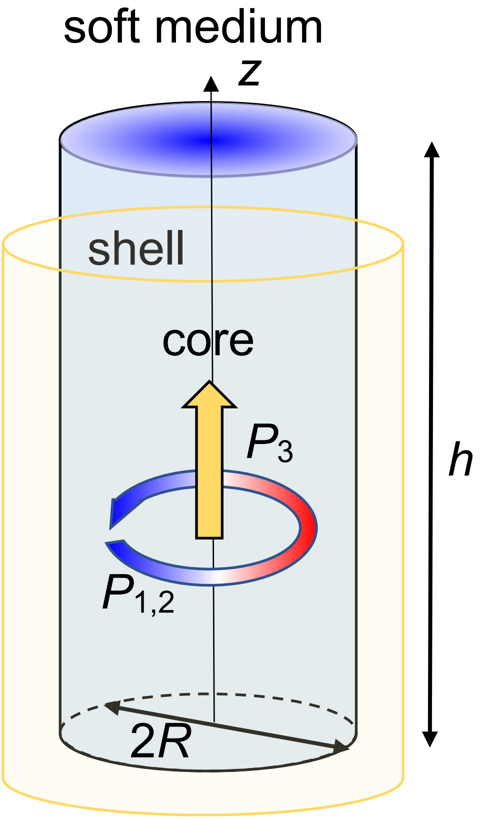

FIGURE 1. A cylindrical ferroelectric nanoparticle (core) of radius R, covered with a paraelectric shell with a screening length of 1 nm, placed in an isotropic elastically soft effective medium. The direction of axial polarization P_3 is shown by the straight orange arrow, and lateral components$P_{1,2}$ are shown by the curled red-blue arrow to highlight their vortex-type structure.

The LGD free energy functional G of the nanoparticle core includes a Landau energy – an expansion on powers of 2-4-6 of the polarization (P_i), G_{Landau}; a polarization gradient energy, G_{grad}; an electrostatic energy, G_{el}; an elastic, electrostriction contribution G_{es}, a flexoelectric contribution, G_{flexo}; and a surface energy, G_S. It has the form [42]:

$$G = G_{Landau} + G_{grad} + G_{el} + G_{flexo} + G_{flexo} + G_S, \tag{1a}$$

$$G_{Landau} = \int_{V_C} d^3r \left[a_i P_i^2 + a_{ij} P_i^2 P_j^2 + a_{ijk} P_i^2 P_j^2 P_k^2\right], \tag{1b}$$

$$G_{grad} = \int_{V_C} d^3r \frac{g_{ijkl}}{2} \frac{\partial P_i}{\partial x_j} \frac{\partial P_k}{\partial x_l}, \tag{1c}$$

$$G_{el} = -\int_{V_C} d^3r \left(P_i E_i + \frac{\varepsilon_0 \varepsilon_b}{2} E_i E_i\right), \tag{1d}$$

$$G_{es} = -\int_{V_C} d^3r \left(\frac{s_{ijkl}}{2} \sigma_{ij} \sigma_{kl} + Q_{ijkl} \sigma_{ij} P_k P_l\right), \tag{1e}$$

$$G_{flexo} = -\int_{V_C} d^3r \frac{F_{ijkl}}{2} \left(\sigma_{ij} \frac{\partial P_k}{\partial x_l} - P_k \frac{\partial \sigma_{ij}}{\partial x_l}\right), \tag{1f}$$

$$G_S = \frac{1}{2} \int_S d^2r \, a_{ij}^{(S)} \, P_i P_j. \tag{1g}$$

Here V_C is the core volume. The coefficient a_i linearly depends on temperature T, $a_i(T) = \alpha_T[T - T_C]$, where α_T is the inverse Curie-Weiss constant and T_C is the ferroelectric Curie temperature renormalized by electrostriction and surface tension [43]. Tensor components a_{ij} are regarded as temperature-independent. The tensor a_{ij} is positively defined if the ferroelectric material undergoes a second order transition to the paraelectric phase and negative otherwise. The higher nonlinear tensor a_{ijk} and the gradient coefficients tensor g_{ijkl} are positively defined and regarded as temperature-independent. In Eq.(1e), σ_{ij} is the stress tensor, s_{ijkl} is the elastic compliances tensor, and Q_{ijkl} is the electrostriction tensor. In the Lifshitz invariant, Eq.(1f), F_{ijkl} is the flexoelectric tensor.

Euler-Lagrange equations obtained from the variation of the free energy (1), mathematical formulation of the electrostatic and elastic sub-problem, and FEM details are given in **Appendix A** of **Supplementary Materials**. The ferroelectric, dielectric, and elastic properties of the $BaTiO_3$ core are given in **Table I**.

Table I. LGD coefficients and other material parameters of $BaTiO_3$ nanocylinders

Coefficient	Numerical value
$\varepsilon_{b,e}$	$\varepsilon_b = 7$ (core background), $\varepsilon_e = 10$ (surrounding)
a_i (in mJ/C^2)	$a_1 = 3.34(T–381)\cdot10^5$, $\alpha_T = 3.34\cdot10^5$ ($a_1 = –2.94\cdot10^7$ at 298 K)
a_{ij} (in m^{5}J/C^4)	$a_{11} = 4.69(T–393)\cdot10^6–2.02\cdot10^8$, $a_{12} = 3.230\cdot10^8$, ($a_{11} = –6.71\cdot10^8$ at 298 K)
a_{ijk} (in m^{9}J/C^6)	$a_{111} = –5.52(T-393)\cdot10^7+2.76\cdot10^9$, $a_{112} = 4.47\cdot10^9$, $a_{123} = 4.91\cdot10^9$ (at 298 K $a_{111} = 82.8\cdot10^8$, $a_{112} = 44.7\cdot10^8$, $a_{123} = 49.1\cdot10^8$)
Q_{ij} (m^4/C^2)	Q_{11}=0.11, Q_{12}= -0.043, Q_{44}=0.059
s_{ij} (in 10^{-12} Pa^{-1})	s_{11}=8.3, s_{12}= –2.7, s_{44}=9.24
g_{ij} (in 10^{-10}m^{3}J/C^2)	g_{11}=5.0, g_{12}= –0.2, g_{44}= 0.2
F_{ij} (in 10^{-11}m^3/C) f_{ij} (in V)	$F_{11} = 2.4$, $F_{12} = 0.5$, $F_{44} = 0.06$ (these values are recalculated from the values $f_{11} = 5.1$, $f_{12} = 3.3$, $f_{44} = 0.065$ V calculated in [44] The equality $F_{44} = F_{11} - F_{12}$ is valid in the isotropic case.
v_{ijklm}	0 (since its characteristic values are unknown for $BaTiO_3$ and other perovskites)
$a_i^{(s)}$	0 (that corresponds to the so-called natural boundary conditions)
$\beta_T^{(c)}$(in 10^{-6}K^{-1})	9.8 (thermal expansion coefficient)
$a_{cubic}^{(c)}$ (in Å)	4.035 Å lattice constant at 1000 °C
R and h (in nm)	$R = 10$ (vary from 2 to 20 nm), $h = 80$ (vary from 8 to 160 nm)

B. Simulation Details

Electrical boundary conditions. We consider the case when the surface of the core is covered by an elastically soft ultrathin semiconductor shell with a screening length $\Lambda \sim 1$ nm. The coverage can be artificial or natural, where in the latter case it would originate from the polarization screening by surrounding media. Note that a screening length larger than 0.1 nm weakly effects the core domain structure, in this case the screening acts as an electrical open-circuit condition. Thus, we impose an electrical open-circuit condition at the cylinder ends to make the vortex-type polarization energetically favorable.

Initial conditions, shape, and gradient effects variability. We use a four 90-degree domain configuration in the XY-plane with superimposed small random noise as an initial distribution of polarization. These four domains determine the direction of the lateral polarization vorticity. When we used a purely random noise as the initial distribution of polarization, it relaxed to a domain structure resembling 180-degree domains in thin c^+/c^- films, since the depolarization field favors a polarization orientation along the *z*-axis of the elongated cylinder; however, the vorticity of polarization components appears near the cylinder ends (an analog of the flux-closure a-domains in thin films).

FEM, performed for the sharp and rounded ends of a cylindrical core reveals that the distribution of the polarization components depends critically on the curvature radius of the ends (see **Fig. S2** in **Suppl. Mat.**). The increase of the curvature leads to the strong increase of P_3 value and to the simultaneous appearance of c^+/c^- bidomain configuration, which contains flux-closure domains near the spherical ends. Note the dependence of P_3 on the flexoelectric coefficients F_{ij} virtually disappears with the curvature increase.

FEM performed for different values of F_{ij} reveals a high sensitivity of the P_3-distribution to the values of polarization gradient coefficients g_{ij} (see **Fig. S3** in **Suppl. Mat.**). Specifically, the reduction of g_{ij} by a factor of ten leads to the appearance of quasi-stable periodic spot-like P_3-domains. These spot-like domains are insensitive to the value and sign of F_{ij}, if its absolute value is less than $4 \cdot 10^{-11}$m^3/C. The sharp transformation of the spot-like P_3-domains into a stable bidomain configuration with flux-closure domains at the cylinder ends appears at unrealistically high values of F_{ij}. The results presented below are obtained from conducting an FEM analysis on a cylindrical core with sharp ends using the values of g_{ij} listed in **Table I**, because this particular case is the most realistic and has the greatest impact of the flexoelectric coupling.

III. RESULTS OF FINITE ELEMENT MODELING

A. FEM Results at Room Temperature

Images in **Figs. 2a** and **3a** are calculated without electrostriction ($Q_{ij} = 0$) and flexoelectric ($F_{ij} = 0$) couplings between the electric polarization and elastic stresses. For the case a very prolate dipolar kernel oriented along z-axis appears inside the cylindrical core. The kernel has relatively thin 180-degree domain walls, which are mostly uncharged because they are parallel to the kernel axis and cylinder lateral surface. The bound charges appear at the walls only in a small spatial region near the kernel that is contact with the cylinder ends, where the 180-degree walls become counter head-to-head walls. The axial polarization P_3 inside the kernel is high, $P_3 \sim -(20-26)$ μC/cm^2 (this is very close to the bulk polarization of BaTiO$_3$ ~ 26 μC/cm^2), and the surrounding core has relatively small axial polarization of the opposite sign, $P_3 \sim (0-5)$ μC/cm^2. The lateral components of polarization, P_1 and P_2, form a two-dimensional (2D) vortex without a central empty core, because a dipolar kernel evolves instead. The polarization magnitude inside the vortex part of the core is much smaller than the bulk polarization of BaTiO$_3$. The two symmetrical Bloch points with $\boldsymbol{P} = 0$ are located at the junction of the dipolar kernel with the cylinder ends. The "up" or "down" orientation of polarization component P_3 inside the kernel is determined by random noise in the initial conditions.

The direction of the polarization vorticity (see **Fig. 2**, top row) is determined by the initial conditions for the polarization vector (e.g., taken in the form random noise). Images in **Figs. 2b-d** and **3b-e** are calculated for a nonzero electrostriction coupling ($Q_{ij} \neq 0$) and either negative, zero, or positive values of the flexoelectric coefficients F_{ij}. In the presence of electrostriction coupling the dipolar kernel disappears completely (see **Figs. 2c** and **3c**). The flexoelectric effect induces an axial component of polarization with a quadrupolar structure consisting of two oppositely oriented diffuse P_3-domains located near the cylinder ends and separated by a region with $P_3 \approx 0$, but it does not change the direction of polarization vorticity in the radial plane (see **Figs. 2b, 2d** and **3b, 3d**). The diffuseness of the P_3-domain walls is dictated by the need to decrease the depolarization field produced by the bound charges of the head-to-head domain walls. The P_3-domains are located near the cylinder ends, and their length (about 10 nm) and lateral size (about 5 nm) are almost independent on the cylinder length if $h \gg 5$ nm. The component P_3 is very small ($|P_3| \leq 0.4$ μC/cm^2) in comparison with the components $P_{1,2}$, but it increases up to 1.2 μC/cm^2 with the flexoelectric coupling increase (see **Figs. 3e**) and then saturates (see **Figs. 3f**). The axial P_3-domains, which have the opposite direction of polarization, change the direction under the transformation $F_{ij} \rightarrow -F_{ij}$ (compare the position of red and blue diffuse spots of the P_3 distributions in **Fig. 3b** and **3d**), while the distribution of the lateral components $P_{1,2}$ is virtually independent on F_{ij} sign and magnitude (see the top row in **Figs. 2b-2d**).

From now on we will call the revealed quadrupolar-type diffuse domain structure "**flexon**" for the sake of brevity and to underline the flexoelectric nature of its axial polarization. The main effect of the flexoelectric coefficients sign change is the reorientation of the flexon axial polarization. The flexoelectric coupling changes the structure of the polarization orientation (see the bottom row in **Figs. 2b-2e**), but practically has no effect on the polarization magnitude in the flexon (see the middle row in **Figs. 3b-3e**). As a matter of fact, the direction of polarization vector rotation in the XY-plane is independent on the F_{ij} sign.

The polarization structures at the wire ends shown in **Fig. 2b-2d** and **Fig. 2b-2d** display localized chiral structures, which have different chirality on opposite ends of the wire and change their chirality upon reversal of the sign of the flexoelectric coupling constant.

To understand the chirality change, in **Appendix C** we derived an approximate analytical expression for the polarization distribution inside the flexon:

$$P_1(\rho,\varphi,z) \approx p(\rho,z)\sin\varphi, \qquad P_2(\rho,\varphi,z) \approx -p(\rho,z)\cos\varphi, \tag{2a}$$

$$P_3(\rho,\varphi,z) \approx \frac{\frac{Q_{44}}{s_{44}}p(\rho,z)[u_{13}(\rho,\varphi,z)\sin\varphi - u_{23}(\rho,\varphi,z)\cos\varphi] - \frac{F_{11}-F_{44}-F_{12}}{s_{11}-s_{12}}\frac{\partial}{\partial z}u_{33}(\rho,\varphi,z)}{2\left[a_1 - \frac{Q_{11}+2Q_{12}}{s_{11}+2s_{12}}p^2(\rho,z) - \frac{Q_{11}-Q_{12}}{s_{11}-s_{12}}u_{33} + \left[g_{11} + (F_{11}-F_{44}-F_{12})\frac{F_{11}-F_{12}}{s_{11}-s_{12}}\right]L_C^z + g_{44}L_C^x\right]}, \tag{2b}$$

where $\{\rho,\varphi,z\}$ are cylindrical coordinates, the function $p(\rho,z)\sim\tanh\left(\frac{\rho}{L_C^x}\right)$, L_C^x and L_C^z are lateral and axial correlation lengths. The functions $u_{ij}(\rho,\varphi,z)$ are elastic strains, s_{ij} are elastic compliances; Q_{ij} are electrostriction tensor components, g_{ij} are polarization gradient coefficients written in Voight notations. From Eq.(2b), the axial part of the flexon polarization is proportional to $-\frac{F_{11}-F_{44}-F_{12}}{s_{11}-s_{12}}\frac{\partial}{\partial z}u_{33}(\rho,\varphi,z)$, and this proportionality along with **Fig. S6** qualitatively describes the curves' behavior in **Fig. 3f.**

In order to quantify the chirality of the polarization structure and its variation along the cylinder axis, in **Appendix D** we calculate the topological index $n = \frac{1}{4\pi}\int_S \vec{p}\left[\frac{\partial\vec{p}}{\partial x}\times\frac{\partial\vec{p}}{\partial y}\right]dxdy$ [45] of the unit polarization orientation $\vec{p} = \frac{\vec{P}}{P}$ for the integration over the cylinder cross-section $\{x,y\}$. For the case of $P_3(\rho = R, z) \rightarrow 0$, z-dependence of the topological index is

$$n(z) = -\frac{P_3(\rho=0,z)}{2P(\rho=0,z)} \cong -\frac{\mathrm{sign}[f]z}{2\sqrt{1+(z^2/B)}}. \tag{3}$$

Here $\mathrm{sign}[f]$ is the sign of the flexoelectric coefficients F_{ij}, B is a positive constant, which depends on the absolute value of $|F_{ij}|$. $n(z)$ is a normalized profile of $P_3(\rho = 0,z)$, and so

$n(z) = 0$ for $F_{ij} = 0$, and its sign is defined by the sign of F_{ij}. The dependence $n(z)$ is shown in **Fig. 3g** and **Fig. S7a** for zero, positive, and negative F_{ij}. Since the value $P(0,z)$ is very close to the $P_3(0,z)$ near the cylinder ends (see **Fig. S7a** and **S7b**), and $P_3(0,z)$ vanishes in the central part of a nanoparticle, the topological index continuously changes from -½ to +½ with a z-coordinate change from one cylinder end to the other. The result clearly shows the localization of the chiral structures – the flexons – at the ends of the wires. The topological index, which can be interpreted as the degree to which a structure is chiral, changes sign from one and to the other, and changes sign upon reversal of the sign of F_{ij}. It also increases in magnitude with increasing absolute value of $|F_{ij}|$. These properties make obvious the clear correlation between the flexoelectric effect and the formation of chiral polarization structures.

In contrast to the topological index, the toroidal moment, $\vec{M} = \frac{1}{V}\int_V [\vec{P} \times \vec{r}] d^3r$, appears almost the same for zero, positive, and negative flexoelectric tensor coefficients. The reason $\vec{M}$ is, for the most part, unaffected by the flexoelectric effect is that $\vec{M}$ is equal to the integral of polarization magnitude $p(\rho,z)$, namely $\vec{M} \approx \vec{e_z}\frac{2}{R^2}\int_0^R p(\rho,z)\rho d\rho$, where the magnitude $p(\rho,z)$ is nearly independent on the flexoelectric coupling (see e.g., **Fig. S4,** the middle row).

The new type of isolated chiral polarization structures, which we call flexons, display features of a three-dimensional meron. In this sense, the polarization vortex in the XY-plane can be interpreted as the Bloch-like transition region of a meron connecting polarization directions of opposite P_3 sign in the core region and in the outer cylindrical shell (see **Fig. 2**). The flexon polarization $\vec{P}$ develops a characteristic drop-shape with a **chiral** structure localized near the surfaces of the cylinder that is reminiscent of the chiral-bobber state found in non-centrosymmetric magnetic films [46] and nanoparticles [47]. It is worth noting that similar, skyrmion-like configurations at the ends of cylindrical nanowires have also been predicted analytically [48] and numerically [49] in the case of non-chiral ferromagnetic materials, but only in the form of transient configurations appearing during the dynamic magnetization reversal process. Here, the skyrmion-like polarization structures appear as stable states in the ferroelectrics, owing to a chiral-symmetry breaking effect of the flexoelectric coupling. In contrast to previous findings [50, 51, 52], the flexon structure is chiral [53] and almost uncharged because $div\vec{P} \cong 0$ (see **Fig. S6b** in **Appendix C**).

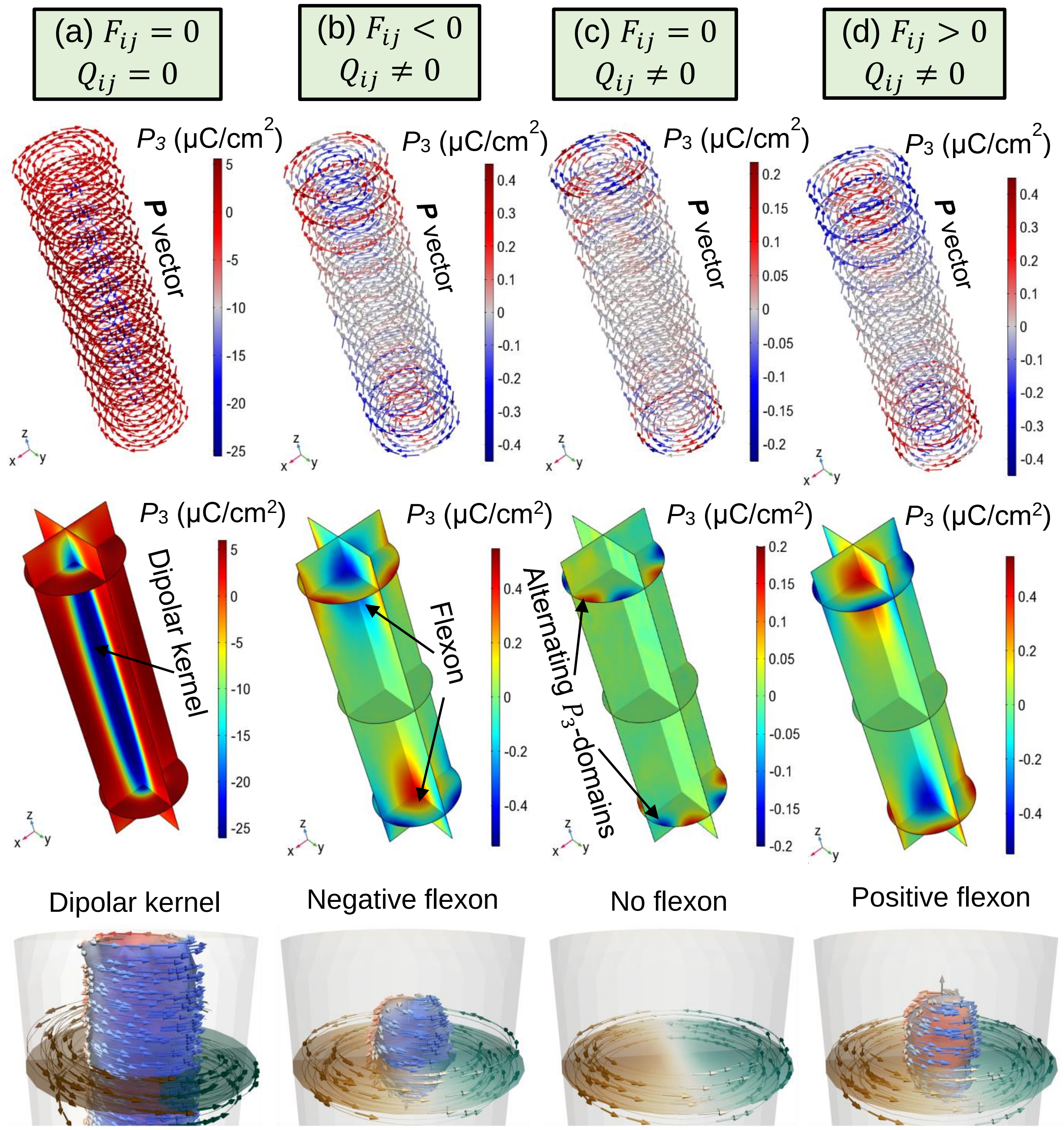

FIGURE 2. Distribution of the polarization vector **P** (the **top row**), its component P_3 (the **middle row**), and the isosurfaces of polarization components (the **bottom row**) inside a cylindrical nanoparticle. The images are calculated without electrostriction ($Q_{ij} = 0$) and flexoelectric ($F_{ij} = 0$) couplings **(a)**; with electrostriction coupling ($Q_{ij} \neq 0$) and negative **(b)**, or zero **(c)**, or positive **(d)** values of flexoelectric coefficients F_{ij}. The **top row:** arrows show the distribution of polarization vector **P**. The arrow color corresponds to the value of P_3 (in red-blue scale). The **middle row**: distribution of P_3 in three different cross-sections of the nanoparticle core. The **bottom row** shows a magnified view on the flexon structure. The values of F_{ij} and all other parameters are given in **Table I**, $T = 300$ K.

The maximal (P_{max}) and minimal (P_{min}) values of P_3 occur at $F_{ij} = 0$ (see the red and blue curves in **Fig. 3f**). The values P_{max} and P_{min} are even functions of the flexoelectric coupling strength f, where $F_{ij} = fF_{ij}^0$ and the reference values of F_{ij}^0 are given in **Table I**. The extremal (maximal or minimal) value P_e in the center of the diffuse axial P_3-domain is an odd function of f, which is zero at $F_{ij} = 0$ (see the green curve in **Fig. 3f**).

Note that the P_e value frequently differs from P_{max} and P_{min} values due to the presence of the small sixteen P_3-domains localized near the top and bottom junction of cylindrical sidewall with the cylinder ends. The polarization direction alternates in these 180-degree domains: four "up" domains alter with four "down" domains at each junction. These alternating P_3-domains are not the part of flexon, because they are induced by the electrostriction coupling. Their structure depends weakly on the flexoelectric coupling strength f, if f is small. However, the shape of each domain significantly changes and the size of each domain moderately increases as $|F_{ij}|$ increases (compare **Fig. 3d** and **Fig. 3e**). The change of polarization direction occurs in each of the 16 alternating P_3-domains at $F_{ij} \rightarrow -F_{ij}$.

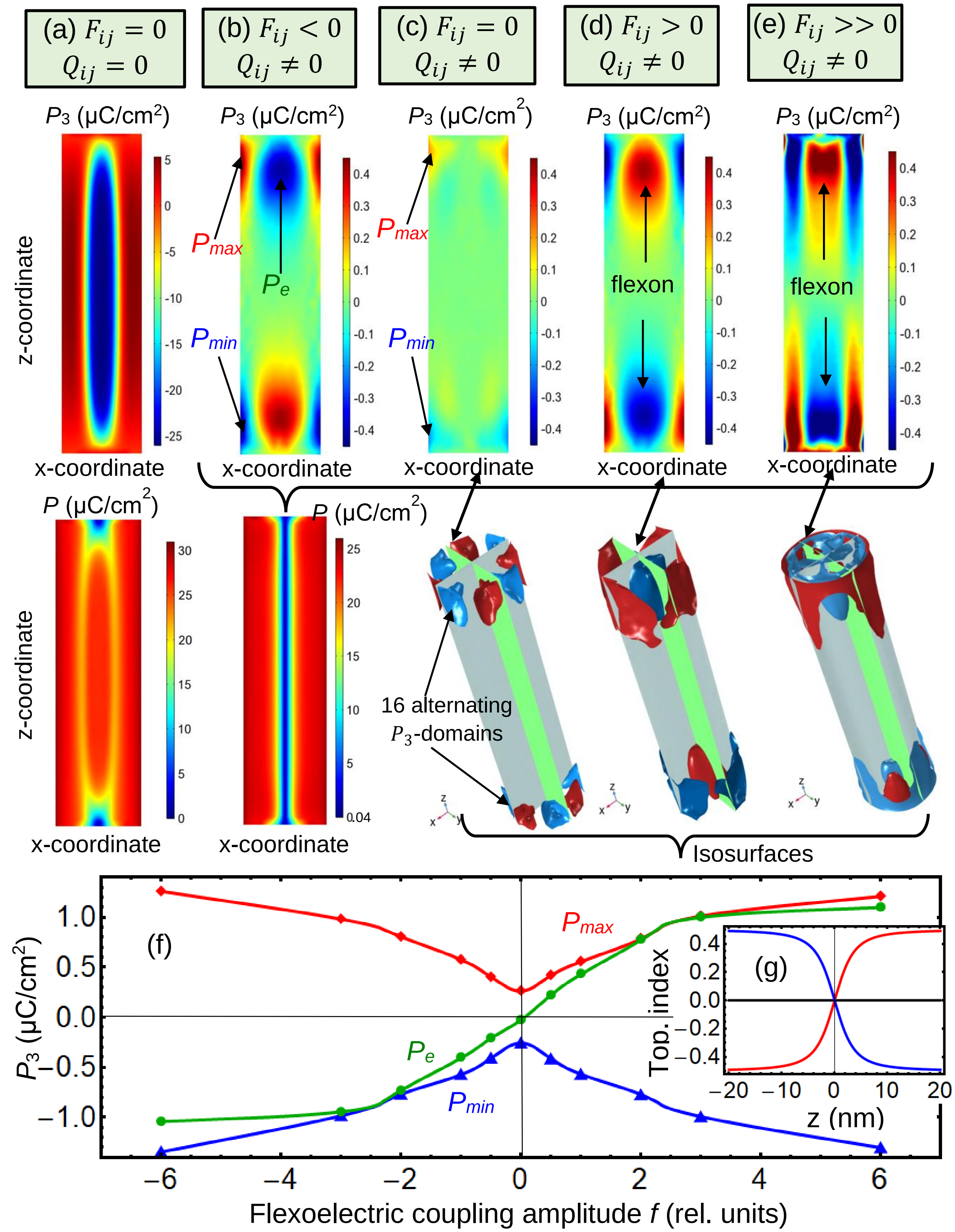

FIGURE 3. Distribution of the polarization component P_3 (the **top row**), polarization magnitude in the XZ cross-section of the nanoparticle, and isosurfaces of polarization components $P_1 = 0$ (gray), $P_2 = 0$ (green), P_3 =+0.1μC/cm^2 (red), and P_3 =–0.1μC/cm^2 (blue) (the **middle row**). Images are calculated without electrostriction ($Q_{ij} = 0$) and flexoelectric ($F_{ij} = 0$) coupling **(a)**; with electrostriction coupling

($Q_{ij} \neq 0$) and negative **(b)**, zero **(c)**, positive **(d)**, or high positive **(e)** values of flexoelectric coefficients F_{ij}. The **bottom part (f)** is the dependence of the maximal (red curve, P_{max}) and minimal (blue curve, P_{min}) values of P_3 on the relative amplitude of the flexoelectric coupling strength f. The green curve is the extremal (maximal or minimal) value P_e in the center of the top axial P_3-domain. Here $F_{ij} = fF_{ij}^0$, the values of F_{ij}^0 and all other parameters are given in **Table I**, $T = 300$ K. The Z-profile of the polarization topological index $n(z)$ is shown in the inset **(g)** for zero (black line), positive (red curve), and negative (blue curve) F_{ij}.

As a rule, the flexoelectric tensor component F_{44} is either poorly known from experiments or ill-defined from ab initio calculations; therefore, we can vary it over a wide range to see whether the flexoelectric coupling anisotropy has any influence on the domain morphology. FEM results are shown in **Fig. 4.** The top and middle rows illustrate that the P_3 distribution changes very strongly when F_{44} varies from high negative to high positive values, while the other components of the flexoelectric tensor are fixed and equal to the tabulated values $F_{11} =$ 2.4 $\cdot 10^{-11}$m^3/C and $F_{12} = 0.5 \cdot 10^{-11}$m^3/C.

The flexon contains two pronounced axial domains located near the cylinder ends, which have thick diffuse domain walls and opposite polarization directions, and exist at high negative (**Fig. 4a**) and high positive (**Fig. 4e**) F_{44} values. The P_3-domains become smaller and more diffuse with a decrease of $|F_{44}|$; but they are still visible and practically do not change their shape, size, or polarization distribution for small $|F_{44}|$ values over the range $|F_{44}| \leq 0.06$ (**Fig. 4b**). The flexon becomes faint and almost disappears when F_{44} approaches the value $F_{44} = F_{11} - F_{12} = 1.9 \cdot 10^{-11}$ m^3/C corresponding to the isotropic symmetry of F_{ij} (**Fig. 4c**). The value will be referred to as "isotropic" below. The "anisotropic" positive values $0.06 \leq F_{44} \leq 3 \cdot 10^{-11}$ m^3/C induce a more visible flexon with two diffuse axial domains (**Fig. 4d**).

The dependence of the maximal (red curve, P_{max}) and minimal (blue curve, P_{min}) values of the polarization component P_3 on the relative amplitude f of the flexoelectric coefficient F_{44} is shown in **Fig. 4f**, where $F_{44} = fF_{44}^0$ and $F_{44}^0 = 0.06 \cdot 10^{-11}$ m^3/C. The values P_{max} and P_{min} reach a very diffuse plateau-like minimum and maximum, respectively, at the isotropic value $F_{44} = F_{11} - F_{12}$. The green curve in **Fig. 4f** is the extremal (maximal or minimal) value P_e in the center of the bottom axial P_3-domain. The extremal value P_a in the center of the diffuse P_3-domain changes its sign in the immediate vicinity of the isotropic value $F_{44} = F_{11} - F_{12}$. The values P_{max}, P_{min}, and P_e have no definite parity, because they are neither odd nor even functions of the flexoelectric coefficient F_{44} amplitude f. From **Fig. 4f** we can conclude that the anisotropy of the flexoelectric coupling has a critically influence on the domain morphology in the flexon.

Actually, the axial part of the flexon polarization is proportional to $-\frac{F_{11}-F_{44}-F_{12}}{s_{11}-s_{12}}\frac{\partial u_{33}}{\partial z}$ [see Eq.(2b)], this proportionality along with **Fig. S7** qualitatively describes the curves' behavior in **Fig. 4f.**

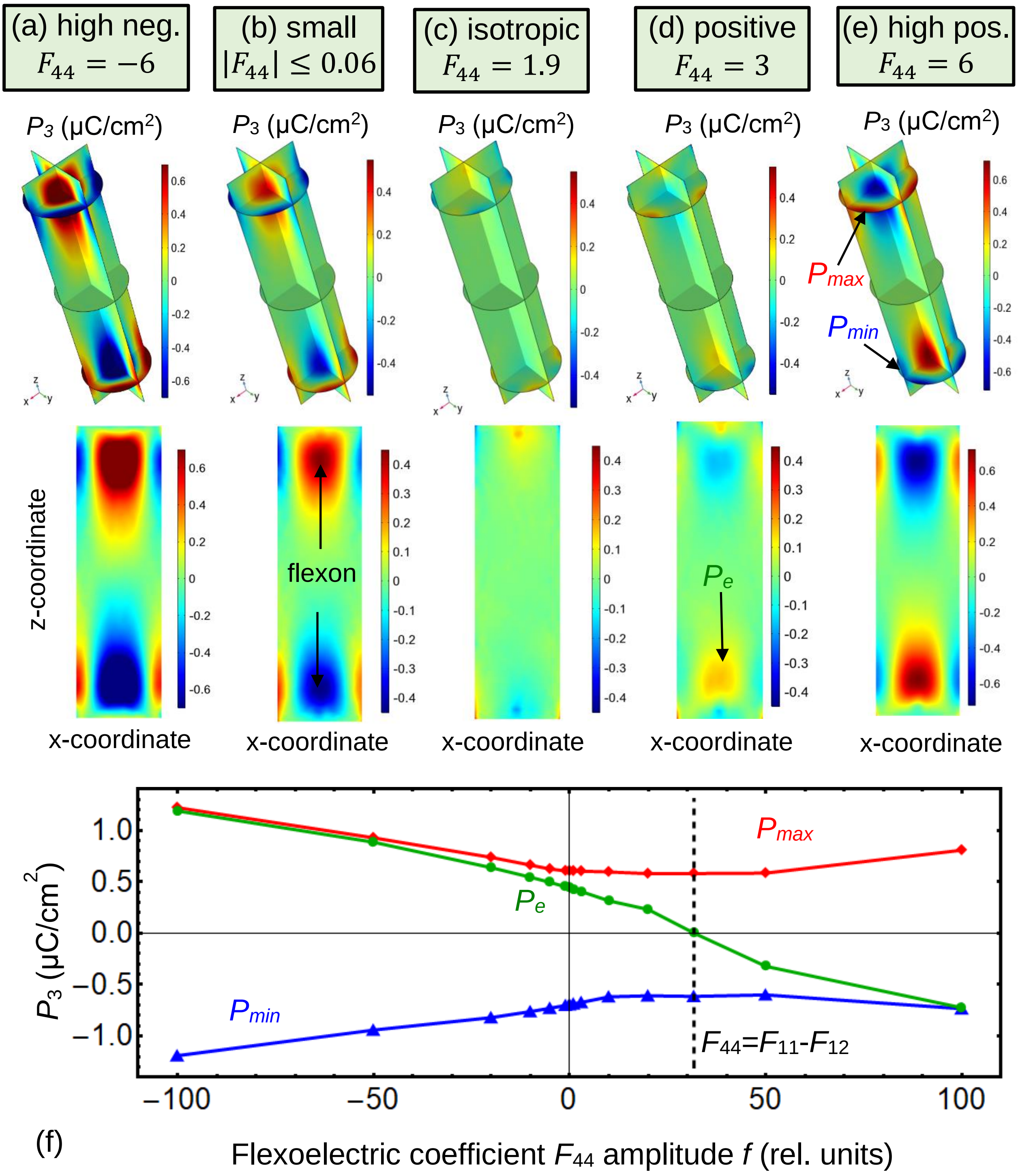

FIGURE 4. Distribution of the polarization component P_3 in three different cross-sections of the nanoparticle core (the **top row**), and in the XZ cross-section of cylindrical core (the **middle row**). Images are calculated for the fixed values $F_{11} = 2.4 \cdot 10^{-11}$ m^3/C and $F_{12} = 0.5 \cdot 10^{-11}$ m^3/C, while the value of

F_{44} varies from -6 to 6 (in 10^{-11}m^3/C) as indicated in the legends. The **bottom part (f)** is the dependence of the maximal (red curve, P_{max}) and minimal (blue curve, P_{min}) values of P_3 on the relative amplitude f of the flexoelectric coefficient F_{44} in the core. The green curve is the extremal (maximal or minimal) value P_e in the center of the bottom axial P_3-domain. Here $F_{44} = fF^0_{44}$ and $F^0_{44} = 0.06 \cdot 10^{-11}$ m^3/C. The electrostriction coupling coefficients Q_{ij} and all other parameters are listed in **Table I**, $T = 300$ K.

The revealed flexon presents a new type of localized, chiral polarization structure induced by a flexoelectric coupling. As we mentioned in the introduction, homochiral interactions in ferroelectrics are not yet firmly established, even though chiral polarization structures, such as ferroelectric skyrmions, have been predicted theoretically [16] and later observed experimentally [21]. Recent theoretical studies have predicted the existence of a ferroelectric DMI analogous to the magnetic interaction that favors the formation of homochiral helicoidal structures in non-centrosymmetric magnetic materials [25, 41]. Our results show that a flexoelectric coupling provides a possible alternative mechanism for the stabilization of chiral polarization structures. We wish to underline the close conceptual similarity between the derivation of the ferroelectric DMI through Lifshitz invariants [40, 41] and that of the flexoelastic effect, which is described by the Lifshitz invariant in Eq. (1f). This interaction, which couples the electric polarization and elastic strain gradients, is ubiquitous in ferroelectrics. Unlike the ferroelectric DMI, it does not require specific and unusual symmetry properties of the underlying crystal in order to be compatible with the Landau theory of phase transitions. Our findings demonstrate that the flexoelastic effect can provide an energetic interaction resulting in the formation of chiral polarization structures [50, 51].

To verify this analogy, we attempt to convert the Lifshitz invariants into chiral interactions of DMI type. Using $div\vec{P} = 0$ for the uncharged domain structures and making straightforward analytic manipulations for a cubic m3m point symmetry group of the BaTiO$_3$ parent phase, the explicit form of the Lifshitz invariant (1f) is $G_{flexo} \approx \frac{F_{11}-F_{44}-F_{12}}{2}\left(\sigma_{ii}\frac{\partial P_i}{\partial x_i} - P_i\frac{\partial \sigma_{ii}}{\partial x_i}\right)$, where a summation over "i" is performed [see Eqs.(C.8) in **Appendix C**]. The elastic stress σ_{ij} contains a contribution proportional to $Q_{ijkl}P_kP_k$, which originates from the electrostriction coupling. For the P_3-component we determine that the term $\frac{F_{11}-F_{44}-F_{12}}{2}Q_{12}\left((P_1^2 + P_2^2)\frac{\partial P_3}{\partial x_3} - P_3\frac{\partial(P_1^2+P_2^2)}{\partial x_3}\right)$ is present in the Lifshitz invariant (1f). A similar invariant has been discussed in Ref. [40] in the context of incommensurate phases with a defined chirality. This is consistent with our finding of the formation of a flexon induced by the invariant.

B. Temperature Behavior of the Flexon-Type Polarization Distribution

To define the temperature interval, where flexons exist being stable or meta-stable, we performed FEM in the temperature range from 50 K to 400 K using different initial distribution of polarization in a cylindrical core. Typical FEM results are shown in **Fig. 5**, where the columns (a)-(e) correspond to the temperature increase from 240 K to 370 K.

A bidomain configuration of P_3 is stable at temperatures lower than 250 K (see **Figs. 5a**). The bidomain structure has a relatively thin uncharged 180-degree domain wall inside the cylinder, which transforms into a flux-closure domain near the electrically-open cylinder ends (see the top and middle images in **Figs. 5a**). The origin of the flux-closure domain is the core tendency to minimize its electrostatic energy, because a flux-closure domain wall creates much a weaker depolarization field (in fact negligibly small) compared to the field the charged 180-degree domain wall would create. The structure of the P-vector is vertex-like and changes moderately when approaching the surface at $T \leq 240$ K (see the direction of arrows in the bottom image of **Figs. 5a**).

We revealed that an initial four-domain polarization distribution relaxes to a flexon-like domain structure in the temperature range $260\text{ K} < T < 360\text{ K}$ (see the middle row in **Figs. 5b-d**). The structure of the P-vector is vortex-like, which weakly changes when approaching the surface in the same temperature range (see the direction of arrows at the bottom image of **Figs. 5b-d**). A relatively small domain wall broadening exists near the cylinder ends, which can be seen from the polarization magnitude distribution at $260\text{ K} < T < 360\text{ K}$ (see the top images of **Figs. 5b-d**).

The flexon gradually disappears at $T > 370$ K (see the middle image in **Figs. 5e**). The ferroelectric polarization inside the core significantly decreases at $T > 370$ K and completely disappears at $T \sim 400$ K (see the top image in **Figs. 5e**). The lateral components P_1 and P_2 form a vortex-like structure, and their distribution is nearly independent of the coordinate z along the cylinder axis. Hence, the vortex-like structure of the P-vector is insensitive to the surface presence. The structure becomes faint with a temperature increase above 370 K (see how the arrows length decreases in the bottom image of **Figs. 5e**). The flexon-type polarization distribution exists in a relatively wide temperature range $260\text{ K} < T < 360$ K. The axial counter domains inherent to flexons are the most pronounced feature over the narrower range $290\text{ K} < T < 340$ K. The relatively wide temperature range (about 100 K) corresponding to the stability or meta-stability of the flexon-type polarization distribution gives us the hope that the domain morphology can be observed experimentally.

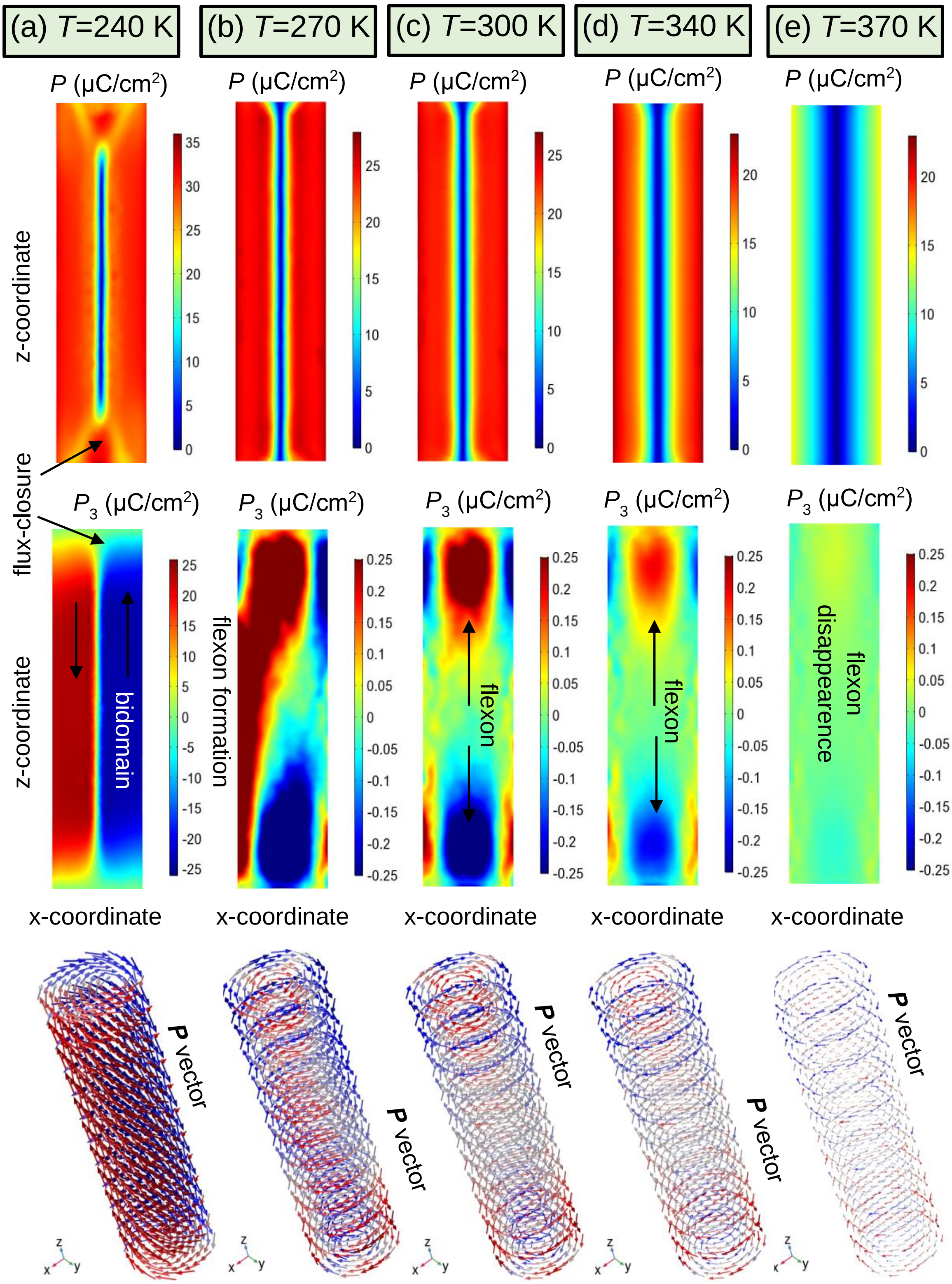

FIGURE 5. Distribution of polarization magnitude P (**top row**) and its component P_3 (**middle row**) in XZ cross-sections of the nanoparticle core**. Bottom row:** distribution of polarization vector **P** shown by arrows colored according to the value of P_3. Different columns are calculated for the temperatures $T = 240, 270, 300, 340,$ and 370 K **(a, b, c, d, e)**. All other parameters are listed in **Table I**.

C. Influence of an External Electric Field on the Flexon Dynamics

The orientation of P_3 can be readily changed by the application of an external electric field. Typical quasistatic hysteresis loops of $P_3(U)$ are shown in **Figs. 6a-d**, where the black loops correspond to the average polarization $\overline{P_3}(U)$; blue and red loops correspond to the minimal ($P_{min}(U)$) and maximal ($P_{max}(U)$) values of $P_3(U)$ at a given voltage U. The loops of $\overline{P_3}(U)$ are very slim, voltage-symmetric (since their shape is symmetrical with respect to the transformation $U \to -U$), and belong to the antiferroelectric type (since they are double loops with $\overline{P_3}(U) = 0$). The loops of $P_{min}(U)$ and $P_{max}(U)$ are strongly voltage-asymmetric and contain two single loops of different shape and size, which we refer to as "major" and "minor" loops. The loop $P_{min}(U)$ is strongly shifted downward, and the loop $P_{max}(U)$ is strongly shifted upward.

The loops in **Figs. 6a-6c** are calculated for nonzero electrostriction coupling coefficients and negative, zero, or positive flexoelectric coupling coefficients F_{ij}. The main difference between the loops shown in **Figs. 6a, 6b,** and **6c**, appear in a horizontal shift (imprint) of the asymmetric loops $P_{min}(U)$ and $P_{max}(U)$, originating from the virtual "flexoelectric" field. The field is proportional to the combination of F_{ij}, and so its direction is defined by the sign of F_{ij}, and it is absent for $F_{ij} = 0$. In the linear approximation, the flexoelectric field is proportional to $(F_{11} - F_{44} - F_{12}) \frac{\partial u_{33}}{\partial z}$, where u_{33} is the component of elastic strain tensor (see **Appendix C** for details). The proportionality partially explains the right shift ($U_{int} > 0$) of the intersection point between major and minor loops calculated for $F_{ij} \leq 0$ (shown in **Figs. 6a-b**) and the left shift of the intersection point calculated for $F_{ij} > 0$ (shown in **Fig. 6c**).

The loops in **Fig. 6d** are calculated without electrostriction ($Q_{ij} = 0$) and flexoelectric coupling ($F_{ij} = 0$). Here the loop of $\overline{P_3}(U)$ is almost indistinguishable from the loops $\overline{P_3}(U)$ shown in **Figs. 6a-6c** for $Q_{ij} \neq 0$**.** The subtle difference is an ultra-small coercivity at $U = 0$, which is absent for the loops in **Figs. 6a-c.** The minor loops of $P_{min}(U)$ and $P_{max}(U)$ are very small in comparison with the major loops, and they are also significantly smaller than the minor loops shown in **Figs. 6a-6c**. The intersection point of major and minor loops corresponds to $U_{int} = 0$.

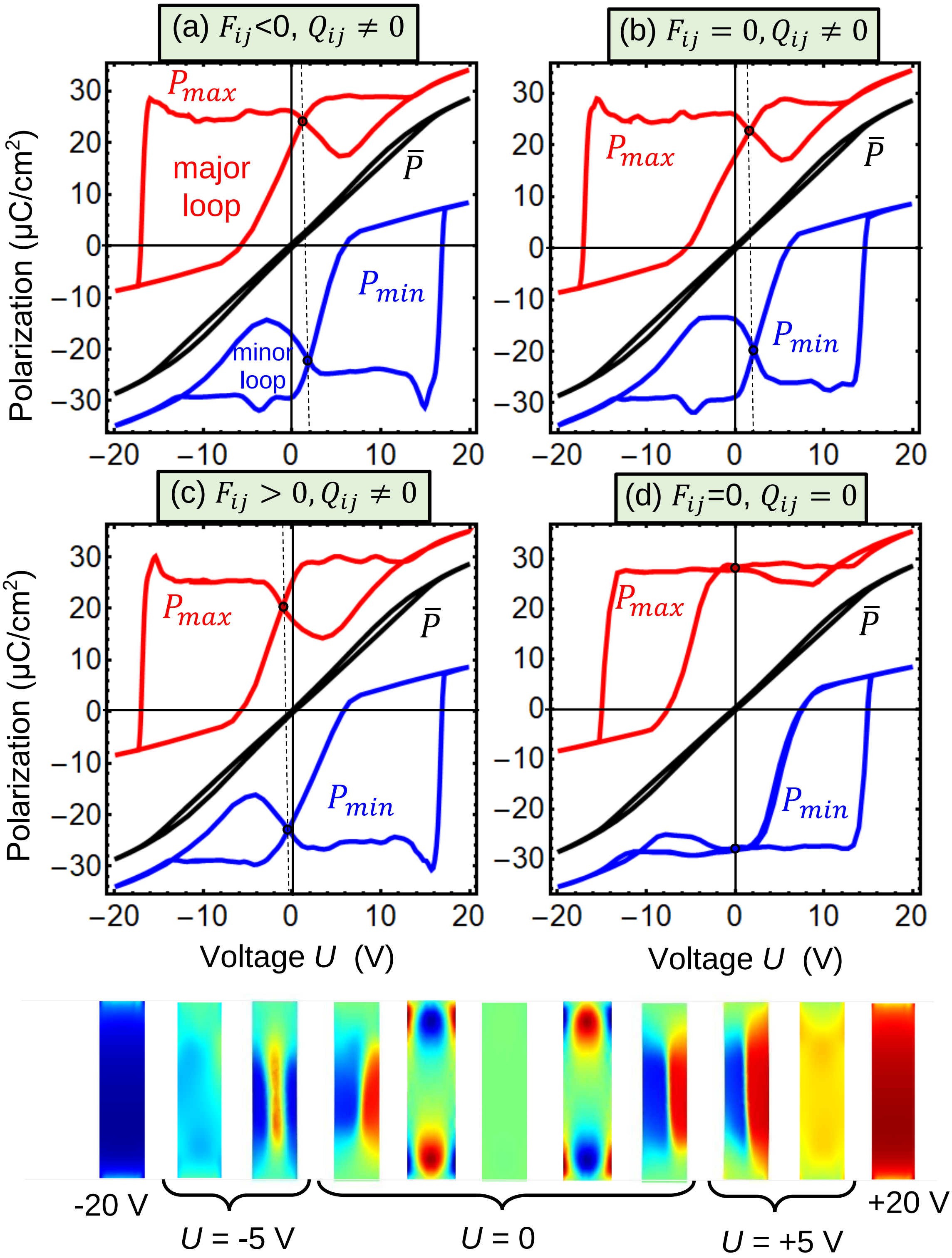

FIGURE 6. Dependence of the average polarization component $\overline{P_3}$ (black loops) and its minimal P_{min} (blue loops) and maximal P_{max} (red loops) values on the applied voltage U. Black dots connected with a vertical dashed line correspond to U_{int}. Plots **(a-d)** are calculated for different values of electrostriction and flexoelectric coupling coefficients, as written in the legends. The plots **(a-c)** are calculated for nonzero electrostriction coupling coefficients ($Q_{ij} \neq 0$) and negative **(a)**, zero **(b)**, or positive **(c)** flexoelectric coupling coefficients F_{ij}. Plot **(d)** is calculated without electrostriction ($Q_{ij} = 0$) and flexoelectric ($F_{ij} =$

0) coupling. Temperature $T = 300\ K$, the distance between the electrodes is 60 nm. All other parameters are listed in **Table I**. The bottom row shows P_3 distributions for different voltages U. Different distributions corresponding to the same U illustrate a rather small hysteresis effect.

The bottom row in **Fig. 6** shows P_3 distributions for different voltages, from which it follows that different P_3 distributions averaged over the core volume correspond to the same average value, $\overline{P_3}(U)$. Thus, the analysis of the hysteresis loops leads to the conclusion that flexons cannot be distinguished from macroscopic (e.g., capacitance) measurements of the average polarization in a homogeneous electric field, they can only be registered by local probing methods using the strong gradient of electric field with a nanoscale resolution, such as piezoresponse force microscopy (**PFM**).

Specifically, the measurements of local vertical displacement by PFM visualize the distribution of $P_3(\vec{r})$ at distances ~ 10 nm from the ends of a nanoparticle, but the resolution procedure for the local piezoresponse of diffuse domains under the surface is far not straightforward [54, 55]. This is because PFM is a near-field method. A complementary tool is the far-field nonlinear optical microscopy (**NOM**) method [17], which has a comparatively much lower resolution than PFM, yet optimum focusing methods and the experimental geometry allow for overcoming the diffraction limit in NOM. For example, second-harmonic generation (SHG) microscopy with a focused beam was successfully used by the community to precisely study semiconductor nanowires [56]. SHG microscopy should also be capable of providing complementary information on the 3D ferroelectric domain structure (being sensitive to $P_{1,2}$ and P_3) by using polarimetry analysis (see, e.g., [57]).

IV. DISCUSSION

Evolving from a four 90-degree domain configuration the flexon-type polarization distribution is metastable, because the antiparallel bidomain-type polarization distribution (evolving from a random noise) has the lowest free energy in a $BaTiO_3$ cylindrical nanoparticle. Corresponding energies are $G_{fl} = -3.6 \cdot 10^{-18}$ J and $G_{bd} = -4.0 \cdot 10^{-18}$ J at room temperature. The energy difference between the states, $\Delta G = 4 \cdot 10^{-19}$ J is much higher (about $100\ k_B T$) than the thermal energy barrier $k_B T$ at room temperature. However, the ratio $\frac{\Delta G}{k_B T}$ strongly decreases with as the temperature increases. The linear relative dielectric permittivity in both states is about 110 at room temperature and strongly increases with temperature.

Our numerical simulations show that a spontaneous off-field transition from the flexon to the bidomain polarization state does not occur. The in-field transition is possible, and its mechanism is discussed in the previous section. Thus, the bidomain and flexon states of a prolate core-shell ferroelectric nanoparticle can be considered as the exited and ground state of a two-level system suitable for information recording. The two-level system can imitate qubits operating in the temperature range where $1 < \frac{\Delta G}{k_B T} < 5$. Furthermore, the bidomain polarization state corresponds to an antiferroelectric-like state of the nanoparticle polarization, which can be represented as two antiparallel nanoscopic dipoles. The flexon is a much more complex achiral vortex-like configuration containing two counter dipole nanodomains with very diffuse relaxor-like polar properties. Thus an ensemble of prolate core-shell ferroelectric nanoparticles, where a given nanoparticle can be either in a flexon or a bidomain state, can be an alternative media for information processing. The media may exhibit unusual properties including antiferroelectric and/or relaxor-like polarization states, which can lead to additional functionalities. Note, that the appearance of the antiferroelectric and relaxor-like glass states, as well as a newly discovered liquid glass state [58] with additional (anti)ferroelectric ordering and other cross-talk effects, are possible in a suspension of the prolate core-shell ferroelectric nanoparticles.

V. CONCLUSIONS

Using a LGD phenomenological approach along with electrostatic equations and elasticity theory, we perform FEM of the electric polarization, the internal electric field, and the elastic stresses and strains in a core-shell cylindrical ferroelectric nanoparticle placed is a very soft elastic medium. FEM, performed for the sharp and rounded ends of a cylindrical $BaTiO_3$ core reveals that the distribution of the polarization components depends critically on the curvature radius of the cylinder ends and is highly sensitive to the values of polarization gradient coefficients.

FEM results, based on room temperature conditions, reveal the quadrupolar-type diffuse domain structure consisting of two oppositely oriented diffuse axial domains located near the cylinder ends and separated by a region with zero axial polarization, which we named “flexon” to underline the flexoelectric nature of its axial polarization. Analytical calculations and FEM prove that the change of flexoelectric coefficients sign leads to a reorientation of the flexon axial polarization. We also reveal that an anisotropy of the flexoelectric coupling critically influences the flexon formation and related domain morphology.

The flexon polarization forms a localized chiral structure resembling a meron. The structure is localized near the cylindrical surface, and its chirality is determined by the sign of the flexoelectric coupling constant. In contrast to previous findings [50, 51], the flexon structure is almost uncharged. While similar chiral structures have been reported in magnets with strong DMI [46], the polarization state discussed here is formed without any ferroelectric counterpart of the DMI [25, 41], but is stabilized by the flexoelectric coupling. It is worth recalling that the flexoelectric coupling – like the DMI – is derived as a Lifshitz invariant (1f) in the context of the Landau theory of phase transitions. The fact that, like the DMI, the flexoelectric coupling stabilizes structures with a specific chirality demonstrates a close analogy between these two interactions [39]. One important difference is that the flexoelectric coupling is ubiquitous in ferroelectrics, whereas the ferroelectric DMI is forbidden by symmetry in most material types [41]. The coupling of the electric polarization and elastic strain gradients could thus be an alternative, and a much more commonly accessible interaction, for the formation of chiral and achiral structures [50, 51].

We find that, in close analogy to the chiral magnetic structures that are stabilized by the DMI in ferromagnets, chiral polarization structures can form as a result of the flexoelectric interaction in strained nanoparticles. Therefore, the comparison of the impact on chirality of the flexoelectric interaction in strained ferroelectrics with the DMI is relevant.

We predict that the flexon-type polarization distribution exists in the temperature range $260\text{ K} < T < 360\text{ K}$. The axial counter domains inherent to flexon are the most pronounced in the narrower temperature range $290\text{ K} < T < 340\text{ K}$. The relatively wide temperature range (about 50 K) corresponding to the stability or meta-stability of the flexon-type polarization distribution give us the hope that the flexons can be observed experimentally.

However, the analysis of the hysteresis loops leads to the conclusion that flexons and other domain configurations cannot be resolved from macroscopic measurements of the average polarization in a homogeneous electric field. Flexons can be reliably observed by the local methods using a strong gradient of electric field, such as PFM, which gives us the information about the distribution of polarization with a nanoscale resolution. Another promising method is resonant elastic soft X-ray scattering, a synchrotron-based method sensitive to chiral polar arrangements through dichroism effects [59, 60]. This method was successfully applied to detect different topological structures, including vortices [59], skyrmions [21], and chiral domain walls [61].

Acknowledgements. A.N.M. acknowledges EOARD project 9IOE063 and related STCU partner project P751. R.H. and S.C.-H. acknowledge funding from the French National Research Agency through contract ANR-18-CE92-0052 “TOPELEC”. V.Y.R. acknowledges the support of COST Action CA17139.

Authors' contribution. A.N.M. and R.H. generated the research idea and stated the problem. A.N.M. performed analytical calculations, analyze FEM results, obtained by E.A.E., prepared figures and wrote the manuscript draft. E.A.E. wrote the codes and performed FEM calculations. R.H., S.C.-H., V.Yu.R., and D.R.E. worked intensively on the results interpretation and manuscript improvement.

REFERENCES

---

1 J. F. Scott, Applications of modern ferroelectrics Science **315**, 954 (2007).

2 K. M. Rabe, C. H. Ahn, and J.-M. Triscone, Editors, *Physics of Ferroelectrics*, 1st ed. (Springer Berlin Heidelberg, 2007).

3 A. K. Tagantsev, L. E. Cross, and J. Fousek, *Domains in Ferroic Crystals and Thin Films*, 1st ed. (Springer New York, NY, 2010).

4 S. V. Kalinin, Y. Kim, D. Fong, and A. N. Morozovska, Surface-screening mechanisms in ferroelectric thin films and their effect on polarization dynamics and domain structures, Rep. Prog. Phys. **81**, 036502 (2018).

5 A. F. Devonshire, Theory of ferroelectrics, Adv. Phys. **3**, 85 (1954).

6 A. Gruverman, M. Alexe, and D. Meier. Piezoresponse force microscopy and nanoferroic phenomena. Nat. Comm. **10**, 1 (2019).

7 J.-J. Wang, B. Wang, and L.-Q. Chen. Understanding, Predicting, and Designing Ferroelectric Domain Structures and Switching Guided by the Phase-Field Method. Ann. Rev. Mater. Res. **49**, 127 (2019).

8 R. G. P. McQuaid, L. J. McGilly, P. Sharma, A. Gruverman, and J. M. Gregg, Mesoscale flux-closure domain formation in single-crystal $BaTiO_3$, Nat. Commun. **2**, 404 (2011).

9 C. T. Nelson, B. Winchester, Y. Zhang, S. J. Kim, A. Melville, C. Adamo, C. M. Folkman, S. H. Baek, C. B. Eom, D. G. Schlom, L. Q. Chen, and X. Pan, Spontaneous vortex nanodomain arrays at ferroelectric heterointerfaces, Nano Lett. **11**, 828 (2011).

10 C.-L. Jia, K. W. Urban, M. Alexe, D. Hesse, and I. Vrejoiu, Direct observation of continuous electric dipole rotation in flux-closure domains in ferroelectric Pb $(Zr, Ti)O_3$, Science, **331**, 1420 (2011).

11 Y. L. Tang, Y. L. Zhu, X. L. Ma, A. Y. Borisevich, A. N. Morozovska, E. A. Eliseev, W. Y. Wang, Y. J. Wang, Y. B. Xu, Z. D. Zhang, and S. J. Pennycook, Observation of a periodic array of flux-closure quadrants in strained ferroelectric $PbTiO_3$ films, Science **348**, 547 (2015).

12 Q. Zhang, L. Xie, G. Liu, S. Prokhorenko, Y. Nahas, X. Pan, L. Bellaiche, A. Gruverman, N. Valanoor, A. Gruverman, and N. Valanoor, Nanoscale bubble domains and topological transitions in ultrathin ferroelectric films, Adv. Mater. **29**, 1702375 (2017).

---

13 E. A. Eliseev, A. N. Morozovska, C. T. Nelson, and S. V. Kalinin. Intrinsic structural instabilities of domain walls driven by gradient couplings: meandering anferrodistortive-ferroelectric domain walls in $BiFeO_3$. Phys. Rev.B, **99**, 014112 (2019).

14 M. J. Han, E. A. Eliseev, A. N. Morozovska, Y. L. Zhu, Y. L. Tang, Y. J. Wang, X. W. Guo, X. L. Ma. Mapping gradient-driven morphological phase transition at the conductive domain walls of strained multiferroic films. Phys. Rev. B, **100**, 104109 (2019).

15 E. A. Eliseev, Y. M. Fomichov, S. V. Kalinin, Y. M. Vysochanskii, P. Maksymovich and A. N. Morozovska. Labyrinthine domains in ferroelectric nanoparticles: Manifestation of a gradient-induced morphological phase transition. Phys. Rev. B **98**, 054101 (2018).

16 Y. Nahas, S. Prokhorenko, J. Fischer, B. Xu, C. Carrétéro, S. Prosandeev, M. Bibes, S. Fusil, B. Dkhil, V. Garcia, and L. Bellaiche, Inverse transition of labyrinthine domain patterns in ferroelectric thin films, Nature **577**, 47 (2020).

17 S. Cherifi-Hertel, H. Bulou, R. Hertel, G. Taupier, K. D. Dorkenoo, C. Andreas, J. Guyonnet, I. Gaponenko, K. Gallo, and P. Paruch, Non-ising and chiral ferroelectric domain walls revealed by nonlinear optical microscopy. Nat. Commun. **8**, 15768 (2017).

18 B. J. Rodriguez, X. S. Gao, L. F. Liu, W. Lee, I. I. Naumov, A. M. Bratkovsky, D. Hesse, and M. Alexe, Vortex polarization states in nanoscale ferroelectric arrays, Nano Lett. **9**, 1127 (2009).

19 N. Balke, B. Winchester, W. Ren, Y. H. Chu, A. N. Morozovska, E. A. Eliseev, M. Huijben, R. K. Vasudevan, P. Maksymovych, J. Britson, S. Jesse, I. Kornev, R. Ramesh, L. Bellaiche, L. Q. Chen, and S. V. Kalinin, Enhanced electric conductivity at ferroelectric vortex cores in $BiFeO_3$. Nat. Phys. **8**, 81 (2012).

20 A. K. Yadav, C. T. Nelson, S. L. Hsu, Z. Hong, J. D. Clarkson, C. M. Schlepütz, A. R. Damodaran, P. Shafer, E. Arenholz, L. R. Dedon, D. Chen, A. Vishwanath, A. M. Minor, L. Q. Chen, J. F. Scott, L. W. Martin, and R. Ramesh, Observation of polar vortices in oxide superlattices, Nature **530**, 198 (2016).

21 S. Das, Y. L. Tang, Z. Hong, M. A. P. P. Gonçalves, M. R. McCarter, C. Klewe, K. X. Nguyen, F. Gómez-Ortiz, P. Shafer, E. Arenholz, V. A. Stoica, S.-L. Hsu, B. Wang, C. Ophus, J.F. Liu, C.T. Nelson, S. Saremi, B. Prasad, A.B. Mei, D.G. Schlom, J. Íñiguez, P. García-Fernández, D.A. Muller, L.Q. Chen, J. Junquera, L.W. Martin, and R. Ramesh, Observation of room-temperature polar skyrmions, Nature **568**, 368 (2019).

22 J. Hlinka, and P. Ondrejkovic. Skyrmions in ferroelectric materials. Solid State Physics, **70**, 143 (2019), Chapter 4 in “Recent Advances in Topological Ferroics and Their Dynamics” Edited by Robert L. Stamps and Helmut Schulthei. Academic Press (2019).

---

23 I. Dzyaloshinsky, A thermodynamic theory of “weak” ferromagnetism of antiferromagnetics, J. Phys. Chem. Solids **4**, 241 (1958).

24 T. Moriya, Anisotropic superexchange interaction and weak ferromagnetism. Phys. Rev. **120**, 91 (1960).

25 H. J. Zhao, P. Chen, S. Prosandeev, S. Artyukhin, and L. Bellaiche. Dzyaloshinskii–Moriya-like interaction in ferroelectrics and antiferroelectrics, Nat. Mater. **20**, 341 (2021).

26 Yu. A. Barnakov, I. U. Idehenre, S. A. Basun, T. A. Tyson, and D. R. Evans. Uncovering the Mystery of Ferroelectricity in Zero Dimensional Nanoparticles. Royal Society of Chemistry, Nanoscale Adv. **1,** 664 *(*2019).

27 M. D. Glinchuk, A. V. Ragulya, and V. A. Stephanovich. Nanoferroics. Dordrecht: Springer (2013).

28 I. S. Vorotiahin, E. A. Eliseev, Q. Li, S. V. Kalinin, Y. A. Genenko and A. N. Morozovska. Tuning the Polar States of Ferroelectric Films via Surface Charges and Flexoelectricity. Acta Materialia **137** (15), 85 (2017).

29 E. A. Eliseev, I. S. Vorotiahin, Y. M. Fomichov, M. D. Glinchuk, S. V. Kalinin, Y. A. Genenko, and A. N. Morozovska. Defect driven flexo-chemical coupling in thin ferroelectric films. Phys. Rev. B **97,** 024102 (2018).

30 G. Catalan, L. J Sinnamon, J. M Gregg, The effect of flexoelectricity on the dielectric properties of inhomogeneously strained ferroelectric thin films, J. Phys.: Condens. Matter **16**, 2253 (2004).

31 G. Catalan, B. Noheda, J. McAneney, L. J. Sinnamon, J. M. Gregg, Strain gradients in epitaxial ferroelectrics, Phys. Rev B **72,** 020102 (2005).

32 M. S. Majdoub, P. Sharma, and T. Cagin, Title, Phys. Rev B **77**, 125424 (2008).

33 F. Ahmadpoor, P. Sharma, Flexoelectricity in two-dimensional crystalline and biological membranes, Nanoscale **7,** 16555 (2015).

34 E. A. Eliseev, A. N. Morozovska, M. D. Glinchuk, and R. Blinc. Spontaneous flexoelectric/flexomagnetic effect in nanoferroics. Phys. Rev. B. **79**, № 16, 165433-1-10, (2009).

35 A. K. Tagantsev, Piezoelectricity and flexoelectricity in crystalline dielectrics, Phys. Rev B, **34**, 5883 (1986).

36 "Flexoelectricity in Solids: From Theory to Applications". Ed. by A. K. Tagantsev and P. V. Yudin, World Scientific (2016).

---

37 B. Wang, Y. Gu, S. Zhang, L.-Q. Chen. Flexoelectricity in solids: Progress, challenges, and perspectives. Progress in Materials Science, **106**, 100570 (2019).

38 A. N. Bogdanov, and D. A. Yablonskii. Thermodynamically stable "vortices" in magnetically ordered crystals. The mixed state of magnets. Zh. Eksp. Teor. Fiz **95**, 178 (1989).

39 A. Bogdanov. On the stability of localized states in nonlinear field models with Lifshitz invariants, Journal of Experimental and Theoretical Physics Letters **68**, 317 (1998).

40 B. A. Strukov and A.P. Levanyuk, Ferroelectric Phenomena in Crystals, Springer 1998.

41 K. C. Erb, and J. Hlinka. "Vector, bidirector, and Bloch skyrmion phases induced by structural crystallographic symmetry breaking." Phys. Rev. B **102,** 024110 (2020).

42 E. A. Eliseev, A. N. Morozovska, R. Hertel, H. V. Shevliakova, Y. M. Fomichov, V. Yu. Reshetnyak, and D. R. Evans. Flexo-Elastic Control Factors of Domain Morphology in Core-Shell Ferroelectric Nanoparticles: Soft and Rigid Shells (http://arxiv.org/abs/2012.00669)

43 J. J. Wang, E. A. Eliseev, X. Q. Ma, P. P. Wu, A. N. Morozovska, and Long-Qing Chen. Strain effect on phase transitions of $BaTiO_3$ nanowires. Acta Materialia **59**, 7189 (2011).

44 I. Ponomareva, A.K. Tagantsev, L. Bellaiche, Finite-temperature flexoelectricity in ferroelectric thin films from first principles, Phys. Rev. B **85**, 104101 (2012).

45 K. Everschor-Sitte, J. Masell, R. M. Reeve, and M. Kläui. Perspective: Magnetic skyrmions—Overview of recent progress in an active research field. J. Appl. Phys. **124**, 240901 (2018).

46 F. N. Rybakov, A. B. Borisov, S. Blügel, and N. S. Kiselev. New type of stable particle-like states in chiral magnets. Phys. Rev. Lett. **115**, 117201 (2015).

47 S. A. Pathak, and R. Hertel, Three-dimensional chiral magnetization structures in FeGe nanospheres. Phys.Rev. B **103**, 104414 (2021).

48 H. B. Braun. Nucleation in ferromagnetic nanowires—magnetostatics and topology. J. Appl. Phys. **85**, 6172 (1999).

49 R. Hertel J. and J. Kirschner, Magnetic drops in a soft-magnetic cylinder. Journal of Magnetism and Magnetic Materials **278**, L291 (2004).

50 P. V. Yudin, A. K. Tagantsev, E. A. Eliseev, A. N. Morozovska and N. Setter. Bichiral structure of ferroelectric domain walls driven by flexoelectricity. Phys. Rev. B **86**, 134102 (2012).

51 E. A. Eliseev, P. V. Yudin, S. V. Kalinin, N. Setter, A. K. Tagantsev and A. N. Morozovska. Structural phase transitions and electronic phenomena at 180-degree domain walls in rhombohedral $BaTiO_3$. Phys. Rev. B **87**, 054111 (2013).

---

52 Y. Gu, M. Li, A. N. Morozovska, Yi Wang, E. A. Eliseev, V. Gopalan, and L.-Q. Chen. Non-Ising Character of a Ferroelectric Wall Arises from a Flexoelectric Effect. Phys. Rev. B **89**, 174111 (2014).

53 We define an achiral structure as one that is equal to its mirror image, and a chiral structure as one that displays a handedness such that it is distinctly different from its mirror image. Systems governed by chiral-symmetry breaking interactions, such as the DMI, favor the formation of chiral structures with one specific handedness. Those systems are sometimes called homochiral.

54 S. V. Kalinin, E. Karapetian, and M. Kachanov, Nanoelectromechanics of piezoresponse force microscopy. Phys. Rev. **B 70**, 184101 (2004).

55 D. A. Scrymgeour and V. Gopalan, Nanoscale piezoelectric response across a single antiparallel ferroelectric domain wall. Phys. Rev. **B 72**, 024103 (2005).

56 G. Bautista, J. Mäkitalo, Ya Chen, V. Dhaka, M. Grasso, L. Karvonen, H. Jiang et al. Second-harmonic generation imaging of semiconductor nanowires with focused vector beams. Nano Lett. **15**, 1564 (2015).

57 M. Timofeeva, A. Bouravleuv, G. Cirlin, I. Shtrom, I. Soshnikov, M. Reig Escalé, A. Sergeyev, and R. Grange. Polar second-harmonic imaging to resolve pure and mixed crystal phases along GaAs nanowires. Nano Lett. **16**, 6290 (2016).

58 J. Roller, A. Laganapan, J.-M. Meijer, M. Fuchs, and A. Zumbusch. Observation of liquid glass in suspensions of ellipsoidal colloids. PNAS, **118**, no. 3 (2021).

59 P. Shafer, P. García-Fernández, P. Aguado-Puente, A. R. Damodaran, A. K. Yadav, C.T. Nelson, S. L. Hsu, J. C. Wojdeł, J. Íñiguez, L. W. Martin, and E. Arenholz, Emergent chirality in the electric polarization texture of titanate superlattices. Proceedings of the National Academy of Sciences, **115**, 915 (2018).

60 S. W. Lovesey, G. van der Laan, Resonant x-ray diffraction from chiral electric-polarization structures. Phys. Rev. B **98**, 155410 (2018).

61 J. Y. Chauleau, T. Chirac, S. Fusil, V. Garcia, W. Akhtar, J. Tranchida, P. Thibaudeau, I. Gross, C. Blouzon, A. Finco, and M.Bibes, Electric and antiferromagnetic chiral textures at multiferroic domain walls. Nature Materials, **19**, 386 (2020).

Supplementary Materials to

“Introducing the Flexon - a New Chiral Polarization State in Ferroelectrics”

APPENDIX A. Mathematical Formulation of the Problem and FEM Details

A. Mathematical Formulation of the Problem

We use the Landau-Ginzburg-Devonshire (LGD) approach combined with electrostatic equations, because this method has proven to be successful in establishing the physical origin of anomalies in phase diagrams, determining polar and dielectric properties of ferroelectric nanoparticles [1, 2], and calculating the changes of their domain structure morphology with size reduction [3, 4]. The LGD approach allows for the consideration of various size and surface effects, such as correlation effects and depolarization fields arising in the case of incomplete polarization screening [5], surface bond contraction [6, 7], and intrinsic surface stresses and strains [8, 9, 10].

The LGD free energy functional G additively includes a Landau expansion on powers of 2-4-6 of the polarization (P_i), G_{Landau}; a polarization gradient energy contribution, G_{grad}; an electrostatic contribution, G_{el}; the elastic, electrostriction, flexoelectric contributions, $G_{es+flexo}$; and a surface energy, G_S. It has the form [11, 12, 13]:

$$G = G_{Landau} + G_{grad} + G_{el} + G_{es+flexo} + G_S, \tag{A.1a}$$

$$G_{Landau} = \int_{Vc} d^3r \left[a_i P_i^2 + a_{ij} P_i^2 P_j^2 + a_{ijk} P_i^2 P_j^2 P_k^2\right], \tag{A.1b}$$

$$G_{grad} = \int_{Vc} d^3r \frac{g_{ijkl}}{2} \frac{\partial P_i}{\partial x_j} \frac{\partial P_k}{\partial x_l}, \tag{A.1c}$$

$$G_{el} = -\int_{Vc} d^3r \left(P_i E_i + \frac{\varepsilon_0 \varepsilon_b}{2} E_i E_i\right) - \frac{\varepsilon_0}{2} \int_{Vs} \varepsilon_{ij}^S E_i E_j d^3r - \frac{\varepsilon_0}{2} \int_{Vo} \varepsilon_{ij}^e E_i E_j d^3r, \tag{A.1d}$$

$$G_{es+flexo} = -\int_{Vc} d^3r \left(\frac{s_{ijkl}}{2} \sigma_{ij} \sigma_{kl} + Q_{ijkl} \sigma_{ij} P_k P_l + F_{ijkl}\left(\sigma_{ij} \frac{\partial P_k}{\partial x_l} - P_k \frac{\partial \sigma_{ij}}{\partial x_l}\right)\right) \tag{A.1e}$$

$$G_S = \frac{1}{2} \int_S d^2r \, a_{ij}^{(S)} \, P_i P_j. \tag{A.1f}$$

Here V_c and V_s are the core and shell volume, respectively. The coefficient a_i linearly depends on temperature T, $a_i(T) = \alpha_T[T - T_C]$, where α_T is the inverse Curie-Weiss constant and T_C is the ferroelectric Curie temperature renormalized by electrostriction and surface tension. Tensor components a_{ij} are regarded as temperature-independent. The tensor a_{ij} is positively defined if the ferroelectric material undergoes a second order transition to the paraelectric phase and negative otherwise. The higher nonlinear tensor a_{ijk} and the gradient coefficients tensor g_{ijkl} are positively defined and regarded as temperature-independent. The following designations are used in Eq.(A.1e):

σ_{ij} is the stress tensor, s_{ijkl} is the elastic compliances tensor, Q_{ijkl} is the electrostriction tensor, and F_{ijkl} is the flexoelectric tensor.

For cubic (m3m) point symmetry group of the parent phase the explicit form of the “half” Lifshitz invariant for the flexoeffect is

$$\Delta G_{flexo} = [\sigma_{11}F_{11} + (\sigma_{22} + \sigma_{33})F_{12}]\frac{\partial P_1}{\partial x_1} + [\sigma_{22}F_{11} + (\sigma_{11} + \sigma_{33})F_{12}]\frac{\partial P_2}{\partial x_2} + [\sigma_{33}F_{11} + (\sigma_{11} + \sigma_{22})F_{12}]\frac{\partial P_3}{\partial x_3} + F_{44}\left[\sigma_{12}\left(\frac{\partial P_1}{\partial x_2} + \frac{\partial P_2}{\partial x_1}\right) + \sigma_{13}\left(\frac{\partial P_1}{\partial x_3} + \frac{\partial P_3}{\partial x_1}\right) + \sigma_{23}\left(\frac{\partial P_2}{\partial x_3} + \frac{\partial P_3}{\partial x_2}\right)\right] \quad \text{(A.2)}$$

Allowing for the Khalatnikov mechanism of polarization relaxation [14], minimization of the free energy (A.1) with respect to polarization leads to three coupled time-dependent Euler-Lagrange equations for polarization components inside the core, $\frac{\delta G}{\delta P_i} = -\Gamma\frac{\partial P_i}{\partial t}$, where $i = 1, 2, 3$. The explicit form of the equations for a ferroelectric crystal with m3m parent symmetry is:

$$\Gamma\frac{\partial P_1}{\partial t} + 2P_1(a_1 - Q_{12}(\sigma_{22} + \sigma_{33}) - Q_{11}\sigma_{11}) - Q_{44}(\sigma_{12}P_2 + \sigma_{13}P_3) + 4a_{11}P_1^3 + 2a_{12}P_1(P_2^2 + P_3^2) + 6a_{111}P_1^5 + 2a_{112}P_1(P_2^4 + 2P_1^2P_2^2 + P_3^4 + 2P_1^2P_3^2) + 2a_{123}P_1P_2^2P_3^2 - g_{11}\frac{\partial^2 P_1}{\partial x_1^2} - g_{44}\left(\frac{\partial^2 P_1}{\partial x_2^2} + \frac{\partial^2 P_1}{\partial x_3^2}\right) = -F_{11}\frac{\partial \sigma_{11}}{\partial x_1} - F_{12}\left(\frac{\partial \sigma_{22}}{\partial x_1} + \frac{\partial \sigma_{33}}{\partial x_1}\right) - F_{44}\left(\frac{\partial \sigma_{12}}{\partial x_2} + \frac{\partial \sigma_{13}}{\partial x_3}\right) + E_1 \quad \text{(A.3a)}$$

$$\Gamma\frac{\partial P_2}{\partial t} + 2P_2(a_1 - Q_{12}(\sigma_{11} + \sigma_{33}) - Q_{11}\sigma_{22}) - Q_{44}(\sigma_{12}P_1 + \sigma_{23}P_3) + 4a_{11}P_2^3 + 2a_{12}P_2(P_1^2 + P_3^2) + 6a_{111}P_2^5 + 2a_{112}P_2(P_1^4 + 2P_2^2P_1^2 + P_3^4 + 2P_2^2P_3^2) + 2a_{123}P_2P_1^2P_3^2 - g_{11}\frac{\partial^2 P_2}{\partial x_2^2} - g_{44}\left(\frac{\partial^2 P_2}{\partial x_1^2} + \frac{\partial^2 P_2}{\partial x_3^2}\right) = -F_{11}\frac{\partial \sigma_{22}}{\partial x_2} - F_{12}\left(\frac{\partial \sigma_{11}}{\partial x_2} + \frac{\partial \sigma_{33}}{\partial x_2}\right) - F_{44}\left(\frac{\partial \sigma_{12}}{\partial x_1} + \frac{\partial \sigma_{23}}{\partial x_3}\right) + E_2 \quad \text{(A.3b)}$$

$$\Gamma\frac{\partial P_3}{\partial t} + 2P_3(a_1 - Q_{12}(\sigma_{11} + \sigma_{22}) - Q_{11}\sigma_{33}) - Q_{44}(\sigma_{13}P_1 + \sigma_{23}P_2) + 4a_{11}P_3^3 + 2a_{12}P_3(P_1^2 + P_2^2) + 6a_{111}P_3^5 + 2a_{112}P_3(P_1^4 + 2P_3^2P_1^2 + P_2^4 + 2P_2^2P_3^2) + 2a_{123}P_3P_1^2P_2^2 - g_{11}\frac{\partial^2 P_3}{\partial x_3^2} - g_{44}\left(\frac{\partial^2 P_3}{\partial x_1^2} + \frac{\partial^2 P_3}{\partial x_2^2}\right) = -F_{11}\frac{\partial \sigma_{33}}{\partial \mathrm{x}_3} - F_{12}\left(\frac{\partial \sigma_{11}}{\partial \mathrm{x}_3} + \frac{\partial \sigma_{22}}{\partial \mathrm{x}_3}\right) - F_{44}\left(\frac{\partial \sigma_{13}}{\partial x_1} + \frac{\partial \sigma_{23}}{\partial x_2}\right) + E_3 \quad \text{(A.3c)}$$

The temperature-dependent Khalatnikov coefficient Γ [15] determines the relaxation time of the polarization $\tau_K = \Gamma/|\alpha|$. Consequently, τ_K typically varies in the range (10^{-9} – 10^{-6}) seconds for temperatures far from T_C. As argued by Hlinka et al. [16], we assumed that $g'_{44} = -g_{12}$ in Eqs.(A.4).

The boundary condition for polarization at the core-shell interface $r = R$ accounts for the flexoelectric effect:

$$a_{ij}^{(S)} P_j + \left(g_{ijkl}\frac{\partial P_k}{\partial x_l} - F_{klij}\sigma_{kl}\right) n_j\Big|_{r=R} = 0 \qquad \text{(A.4)}$$

where **n** is the outer normal to the surface, i = 1, 2, 3. In our FEM studies, we use the so-called “natural” boundary conditions corresponding to $a_{ij}^{(S)} = 0$.

The electric field components E_i in Eq.(A.3) are derived from the electric potential φ in a conventional way, $E_i = -\partial\varphi/\partial x_i$. The potential φ_f satisfies the Poisson equation in the ferroelectric cylinder (subscript "f"):

$$\varepsilon_0\varepsilon_b\left(\frac{\partial^2}{\partial x_1^2} + \frac{\partial^2}{\partial x_2^2} + \frac{\partial^2}{\partial x_3^2}\right)\varphi_f = \frac{\partial P_i}{\partial x_i}, \qquad x_1^2 + x_2^2 \leq R \,\cap\, 0 \leq x_3 \leq h, \qquad \text{(A.5a)}$$

The electric potential φ_e in the external region outside the core-shell nanoparticle satisfies the Laplace equation (subscript "e"):

$$\varepsilon_0\varepsilon_e\left(\frac{\partial^2}{\partial x_1^2} + \frac{\partial^2}{\partial x_2^2} + \frac{\partial^2}{\partial x_3^2}\right)\varphi_e = 0, \quad x_1^2 + x_2^2 > R \,\cup\, x_3 < 0 \,\cup\, x_3 > h, \qquad \text{(A.5b)}$$

Equations (A.6) are supplemented with the continuity conditions for electric potential and linear screening conditions for the normal components of the electric displacements at the cylinder surface S [17, 18]:

$$\left(\varphi_e - \varphi_f\right)\big|_S = 0, \;\; \boldsymbol{n}\left(\boldsymbol{D}_e - \boldsymbol{D}_f\right)\big|_S = -\frac{\varphi_f}{\Lambda}. \qquad \text{(A.6a)}$$

The boundary condition (A.6a) corresponds to the surface of the core covered by an ultrathin semiconductor shell with an effective screening length Λ ≥1 nm [19, 20, 21]. Note that a screening length greater than 0.1 nm leads to the domain formation in the core. The case Λ → ∞ corresponds to an electrical open-circuit condition. We impose an electrical open-circuit condition at the cylinder ends to make the vortex-type polarization energetically favorable. Either charges are absent or the applied voltage is fixed at the boundaries of the computation region:

$$\frac{\partial\,\varphi_e}{\partial\,x_l} n_l\Big|_{x=\pm\frac{L}{2}} = 0, \;\; \frac{\partial\,\varphi_e}{\partial\,x_l} n_l\Big|_{y=\pm\frac{L}{2}} = 0, \;\; \varphi_e\big|_{z=+\frac{L}{2}} = 0, \;\; \varphi_e\big|_{z=-\frac{L}{2}} = V_e. \qquad \text{(A.6b)}$$

Elastic equations of state follow from the variation of the energy (A.2e) with respect to elastic stress, $\frac{\delta G}{\delta\sigma_{ij}} = -u_{ij}$. In the oversimplified case

$$s_{ijkl}\sigma_{kl} + Q_{ijkl}P_k P_l + F_{ijkl}\frac{\partial P_l}{\partial x_k} = u_{ij}, \quad 0 < r \leq R, \quad 0 < z \leq h\,, \qquad \text{(A.7a)}$$

$$\sigma_{ij} = c_{ijkl}u_{kl} - q_{ijkl}P_k P_l - f_{ijkl}\frac{\partial P_l}{\partial x_k}, \quad 0 < r \le R, \quad 0 < z \le h \,, \tag{A.7b}$$

where u_{ij} is the strain tensor components related to the displacement components U_i in the following way: $u_{ij} = (\partial U_i/\partial x_j + \partial U_j/\partial x_i)/2$. For cubic (m3m) point symmetry group of the parent phase the strain components are:

$$u_{11} = s_{11}\sigma_{11} + s_{12}(\sigma_{22} + \sigma_{33}) + Q_{11}P_1^2 + Q_{12}(P_2^2 + P_3^2) + F_{11}\frac{\partial P_1}{\partial x_1} + F_{12}\left(\frac{\partial P_2}{\partial x_2} + \frac{\partial P_3}{\partial x_3}\right) \tag{A.8a}$$

$$u_{22} = s_{11}\sigma_{22} + s_{12}(\sigma_{11} + \sigma_{33}) + Q_{11}P_2^2 + Q_{12}(P_1^2 + P_3^2) + F_{11}\frac{\partial P_2}{\partial x_2} + F_{12}\left(\frac{\partial P_1}{\partial x_1} + \frac{\partial P_3}{\partial x_3}\right) \tag{A.8b}$$

$$u_{33} = s_{11}\sigma_{33} + s_{12}(\sigma_{11} + \sigma_{22}) + Q_{11}P_3^2 + Q_{12}(P_2^2 + P_1^2) + F_{11}\frac{\partial P_3}{\partial x_3} + F_{12}\left(\frac{\partial P_1}{\partial x_1} + \frac{\partial P_2}{\partial x_2}\right) \tag{A.8c}$$

$$u_{12} = s_{44}\sigma_{12} + Q_{44}P_1P_2 + F_{44}\left(\frac{\partial P_1}{\partial x_2} + \frac{\partial P_2}{\partial x_1}\right) \tag{A.8d}$$

$$u_{13} = s_{44}\sigma_{13} + Q_{44}P_1P_3 + F_{44}\left(\frac{\partial P_1}{\partial x_3} + \frac{\partial P_3}{\partial x_1}\right) \tag{A.8e}$$

$$u_{23} = s_{44}\sigma_{23} + Q_{44}P_3P_2 + F_{44}\left(\frac{\partial P_2}{\partial x_3} + \frac{\partial P_3}{\partial x_2}\right) \tag{A.8f}$$

Equations (A.8) should be considered along with equations of mechanical equilibrium $\partial\sigma_{ij}(\boldsymbol{x})/\partial x_i = 0$ and compatibility equations $e_{ikl}\, e_{jmn}\partial^2 u_{ln}(\boldsymbol{x})/\partial x_k \partial x_m = 0$, which are equivalent to the mechanical displacement vector U_i continuity [22]. The boundary conditions for elastic stresses are the virtual absence of their normal components at the nanoparticle surface, as the ambient media is regarded absolutely soft.

B. Finite Element Modelling Details

FEM simulations are performed in COMSOL@MultiPhysics software, using electrostatics, solid mechanics, and general math (PDE toolbox) modules. The size of the computational region is not less than 40×40×160 nm^3, and is commensurate with the cubic unit cell constant (about 0.4 nm) of BaTiO$_3$ at room temperature. The minimal size of a tetrahedral element in a mesh with fine discretization is equal to the unit cell size, 0.4 nm, the maximal size is (0.8 – 1.2) nm in the core, 1.6 nm in the shell, and 4 nm in the dielectric medium (see **Fig. S1**). The dependence on the mesh size is verified by increasing the minimal size to 0.8 nm. We verified that this only results in minor changes in the electric polarization, electric field, and elastic stress and strain, such that the spatial distribution of each of these quantities becomes less smooth (i.e. they contain numerical errors in the form of a small random noise). However, when using these larger cell sizes, all significant details remain visible, and more importantly, the system energy remains essentially the same with an accuracy of about 0.1%.

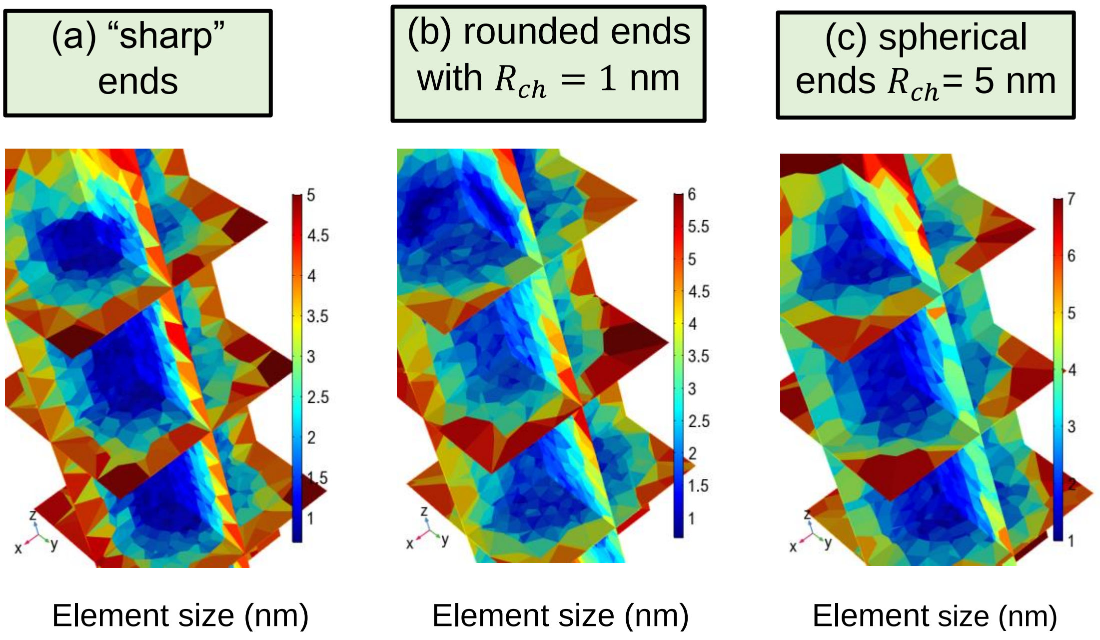

Figure S1. Examples of mesh for the sharp edges (a), rounded edges (b) and rounded caps (c) of the cylindrical nanoparticle. The color corresponds to the size of the mesh elements.

Table S1. LGD coefficients and other material parameters of $BaTiO_3$ nanocylinders

Coefficient	**Numerical value**
$\varepsilon_{b,\,e}$	$\varepsilon_b = 7$ (core background) $\varepsilon_e = 10$ (surrounding)
a_i (in mJ/C^2)	$a_1 = 3.34(T\text{-}381)\cdot10^5$, $\alpha_T = 3.34\cdot10^5$ ($a_1 = -2.94\cdot10^7$ at 298 K)
a_{ij} (in m^5J/C^4)	$a_{11} = 4.69(T\text{-}393)\cdot10^6–2.02\cdot10^8$, $a_{12} = 3.230\cdot10^8$, ($a_{11} = -6.71\cdot10^8$ at 298 K)
a_{ijk} (in m^9J/C^6)	$a_{111} = -5.52(T\text{-}393)\cdot10^7+2.76\cdot10^9$, $a_{112} = 4.47\cdot10^9$, $a_{123} = 4.91\cdot10^9$ (at 298 K $a_{111} = 82.8\cdot10^8$, $a_{112} = 44.7\cdot10^8$, $a_{123} = 49.1\cdot10^8$)
Q_{ij} (m^4/C^2)	Q_{11}=0.11, Q_{12}= -0.043, Q_{44}=0.059
s_{ij} (in 10^{-12} Pa^{-1})	s_{11}=8.3, s_{12}= -2.7, s_{44}=9.24
g_{ij} (in $10^{-10}m^3J/C^2$)	g_{11}=5.0, g_{12}= -0.2, g_{44}= 0.2
F_{ij} (in $10^{-11}m^3/C$) f_{ij} (in V)	$F_{11} = 2.4$, $F_{12} = 0.5$, $F_{44} = 0.06$ (these values are recalculated from [23] values $f_{11} = 5.1$, $f_{12} = 3.3$, $f_{44} = 0.065$ V. The equality $F_{44} = F_{11} - F_{12}$ is valid in the isotropic case.
v_{ijklm}	0 (since its characteristic values are unknown for $BaTiO_3$ and other perovskites)
$a_i^{(s)}$	0 (that corresponds to the so-called natural boundary conditions)
$\beta_T^{(c)}$(in $10^{-6}K^{-1}$)	9.8 (thermal expansion coefficient)
$a_{cubic}^{(c)}$ (in Å)	4.035 Å lattice constant at 1000 °C
R (in nm)	10 (vary from 2 to 20 nm)

Appendix B. Supplementary Figures

FEM, performed for the sharp and rounded ends of cylindrical core at room temperature with nominal values of the flexoelectric tensor components F_{ij} (listed in **Table S1**), reveals that the distribution of the polarization component P_3 depends critically on the curvature radius of the cylinder ends (see **Fig. S2**). The increase of the curvature leads to both a strong increase of the P_3 value and a simultaneous gradual transformation of the multiple edge domains into a bidomain configuration, which contains flux-closure domains at the spherical ends (see the top row in **Fig. S2**). For the sharp and slightly rounded ends, the distribution P_3 becomes much more contrasting with increasing F_{ij}; but the dependence of P_3 on F_{ij} virtually disappears as the curvature increases (compare the top and bottom row in **Fig. S2**). FEM results presented below are performed for the cylindrical core with sharp ends, because this shape is the most sensitive to the flexoelectric coupling.

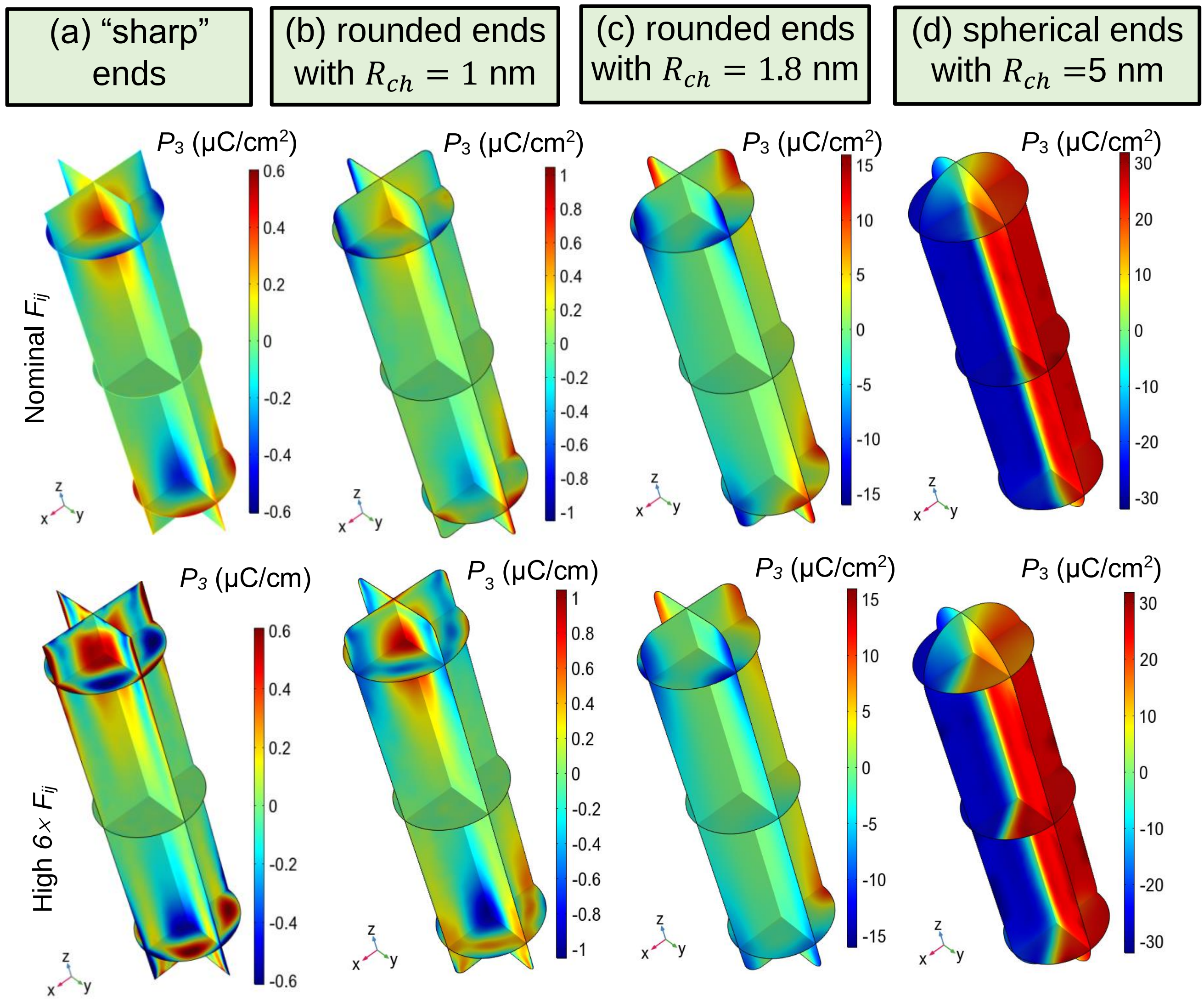

Figure S2. Distribution of the polarization component P_3 in three different cross-sections of the cylindrical nanoparticle with sharp ends **(a)**, rounded ends with curvature R_{ch} =1 nm **(b)** and 1.8 nm **(c)**; and hemispherical ends **(d)**. The values of the flexoelectric coefficients are $F_{11} = 2.4 \cdot 10^{-11}$m^3/C, $F_{12} = 0.5 \cdot 10^{-11}$m^3/C, and $F_{44} = 0.06 \cdot 10^{-11}$m^3/C for the **top row**; $F_{11} = 144 \cdot 10^{-11}$m^3/C, $F_{12} = 3 \cdot 10^{-11}$m^3/C, and $F_{44} = 0.36 \cdot 10^{-11}$m^3/C for the **bottom row.** Temperature $T = 300\ K$. All other parameters are listed in **Table S1**.

FEM, performed for room temperature, zero and nominal values of the electrostriction tensor components Q_{ij}, and different values of F_{ij} reveals the high sensitivity of the P_3-distribution to the values of polarization gradient coefficients g_{ij}. The nominal values of Q_{ij}, F_{ij} , and g_{ij} are listed in **Table S1.** For zero $Q_{ij} = 0$ and $F_{ij} = 0$ the shape of the P_3-distribution is insensitive to the values of the polarization gradient coefficients g_{ij}; the width of 180-degree domain walls is proportional to $\sqrt{g_{44}}$ (compare **Fig. S3a** with **Fig. 2a** in the main text).

For nonzero nominal values of Q_{ij} a factor of 10 decrease of g_{ij} leads to the appearance of quasi-periodic spot-like P_3-domains located near the lateral surface of the cylinder (shown by blue and red spots in the top row of **Figs. S3b-d**) instead of two diffuse axial domains shown in **Fig. S2a**. These spot-like domains are insensitive to the value and sign of F_{ij}, if its absolute value is less than $3 \cdot 10^{-11}$m^3/C (see **Figs. S3b-d**). Corresponding distributions of polarization magnitude P calculated for nonzero Q_{ij} and $|F_{ij}| < 4 \cdot 10^{-11}$m^3/C reveal a twisted central line with quasi-periodically located multiple Bloch points, $P = 0$, whose patterns are shown in the bottom row of **Figs. S3b-d**.

The sharp transformation of the quasi-stable spot-like P_3-domains into a stable bidomain configuration with flux-closure domains at the cylinder ends appears at very high values of F_{ij} (see **Fig. S3e**). FEM results presented below are performed for nominal values of g_{ij} (listed in **Table S1**), because this case is the most realistic and the most sensitive to the flexoelectric coupling.

The distributions of the polarization component P_3 in three different cross-sections of the nanoparticle core, polarization magnitude P in the XZ cross-section of the nanoparticle, and isosurfaces of polarization components $P_{1,2,3}$ are shown in **Fig. S4**. The images are calculated without electrostriction ($Q_{ij} = 0$) and flexoelectric ($F_{ij} = 0$) coupling (**Fig. S4a**); with electrostriction coupling ($Q_{ij} \neq 0$) and negative (**Fig. S4b**), zero (**Fig. S4c**), positive (**Fig. S4d**), or high positive (**Fig. S4e**) values of the flexoelectric coefficients F_{ij}.

The distribution of the polarization component P_3 in three different cross-sections of the nanoparticle core, P_3 distribution XZ cross-section, and isosurfaces of polarization components $P_{1,2,3}$ are shown in **Fig. S5**. Images are calculated for the fixed values $F_{11} = 2.4 \cdot 10^{-11}$m^3/C and $F_{12} = 0.5 \cdot 10^{-11}$m^3/C are, and the value of F_{44} varies from -6 to 6 (in 10^{-11}m^3/C) as indicated in the legends to **Fig. S5a-f**.

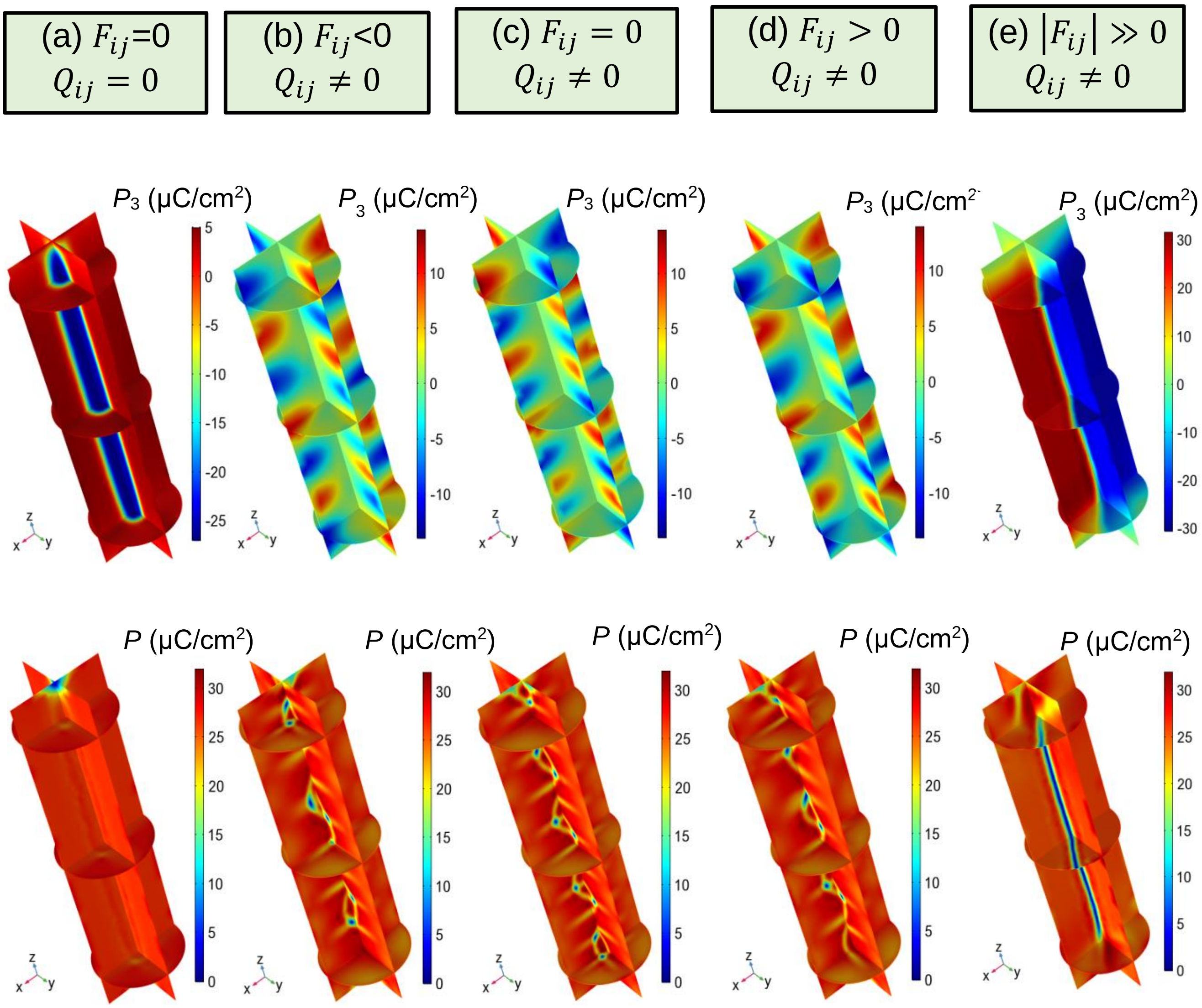

Figure S3. Distribution of the polarization component P_3 (**top row**), and polarization magnitude P (**bottom row**) in three different cross-sections of the nanoparticle core. Different columns are calculated for the different values of electrostriction and flexoelectric coupling coefficients. The following values of gradients are used: $g_{11} = 1 \cdot 10^{-10}$m^3/F, $g_{12} = -0.04 \cdot 10^{-10}$m^3/F, and $g_{44} = 0.04\ 10^{-11}$m^3/F. Temperature $T = 300\ K$. All other parameters are listed in **Table S1**.

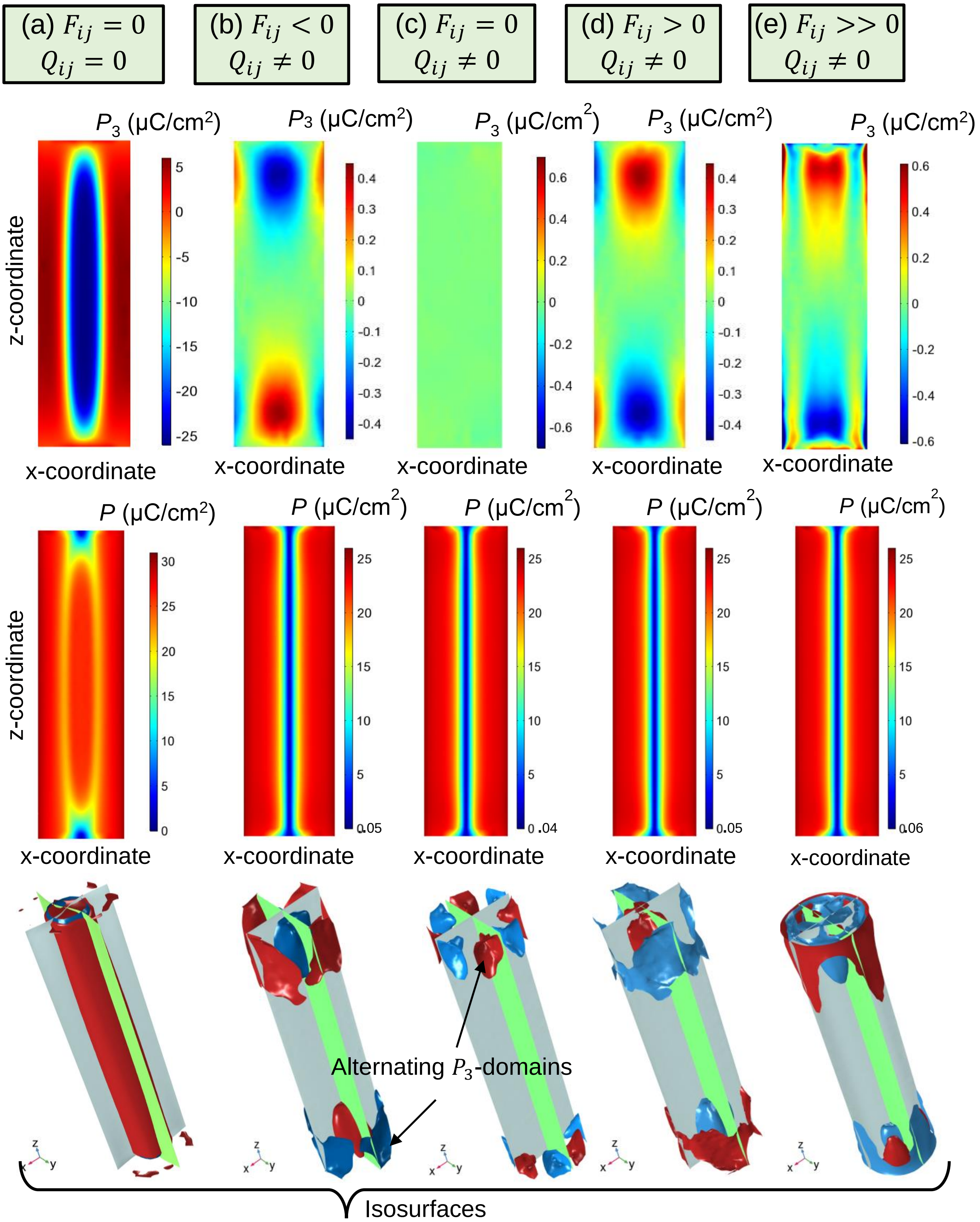

Figure S4. Distribution of the polarization component P$_3$ (the **top row**) and polarization magnitude (the **middle row**) in the XZ cross-section of the nanoparticle. **The bottom row**: isosurfaces of zero polarization components P_1 (gray), P_2 (green), and nonzero $P_3 = \pm 0.1$, ± 0.1, ± 0.2, and ± 0.4 μC/cm^2 (red and blue). Images are calculated without electrostriction ($Q_{ij} = 0$) and flexoelectric ($F_{ij} = 0$) coupling **(a)**; with electrostriction coupling ($Q_{ij} \neq 0$) and negative **(b)**, zero **(c)**, positive **(d)**, or tripled positive **(e)** values of flexoelectric coefficients F_{ij}. Reference values of F_{ij} and all other parameters are given in **Table S1.** Temperature $T = 300\ K$.

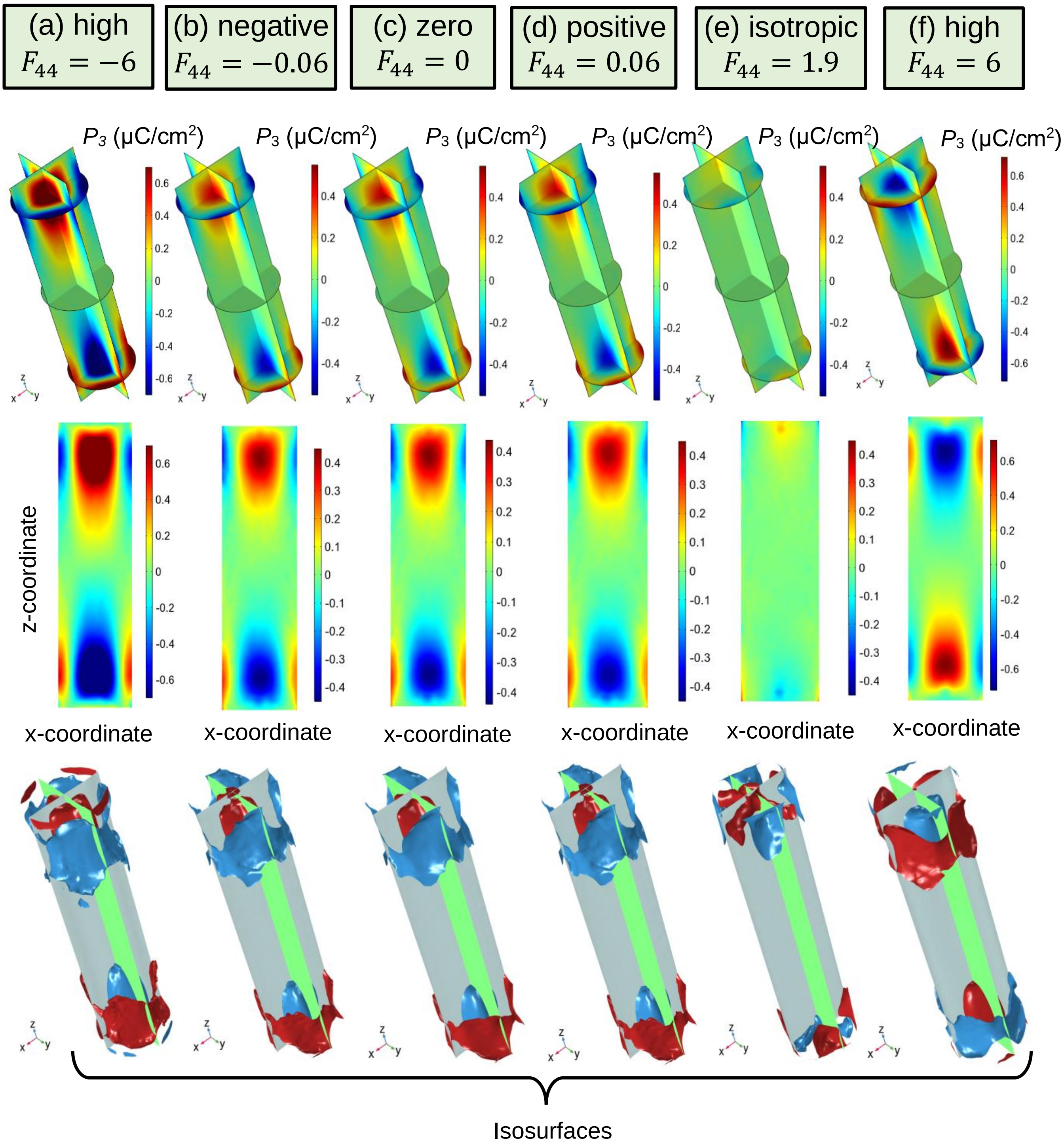

Figure S5. Distribution of polarization component P_3 in three different cross-sections of the nanoparticle core (**top row**), and P_3 in the XZ cross-section of cylindrical core (**middle row**). **Bottom row:** isosurfaces of polarization components P_1 (gray), P_2 (green), and P_3 (red and blue). Zero values correspond P_1 and P_2 isosurfaces, while isosurfaces of P_3 correspond to the values $P_3 = \pm 0.1, \pm 0.2$, and ± 0.4 μC/cm^2 for the images

(a)-(d), **(e),** and **(f)** respectively. The images are calculated for the fixed values $F_{11} = 2.4 \cdot 10^{-11}$m^3/C and $F_{12} = 0.5 \cdot 10^{-11}$m^3/C, while the value of F_{44} varies from -6 to 6 (in 10^{-11}m^3/C) as indicated in the legends. All other parameters are listed in **Table S1**. Temperature $T = 300\ K$.

Appendix C. Approximate Analytical Solution

Since $\frac{\partial \sigma_{i1}}{\partial x_i} = \frac{\partial \sigma_{i2}}{\partial x_i} = \frac{\partial \sigma_{i3}}{\partial x_i} = 0$ in accordance with mechanical equilibrium equations, the right-hand sides in Eqs. (A.3) can be rewritten as:

$$\Gamma \frac{\partial P_1}{\partial t} + 2P_1(a_1 - Q_{12}(\sigma_{22} + \sigma_{33}) - Q_{11}\sigma_{11}) - Q_{44}(\sigma_{12}P_2 + \sigma_{13}P_3) + 4a_{11}P_1^3 + 2a_{12}P_1(P_2^2 + P_3^2) + 6a_{111}P_1^5 + 2a_{112}P_1(P_2^4 + 2P_1^2P_2^2 + P_3^4 + 2P_1^2P_3^2) + 2a_{123}P_1P_2^2P_3^2 - g_{11}\frac{\partial^2 P_1}{\partial x_1^2} - g_{44}\left(\frac{\partial^2 P_1}{\partial x_2^2} + \frac{\partial^2 P_1}{\partial x_3^2}\right) = -(F_{11} - F_{44} - F_{12})\frac{\partial \sigma_{11}}{\partial x_1} - F_{12}\frac{\partial}{\partial x_1} Tr\hat{\sigma} + E_1 \quad \text{(C.1a)}$$

$$\Gamma \frac{\partial P_2}{\partial t} + 2P_2(a_1 - Q_{12}(\sigma_{11} + \sigma_{33}) - Q_{11}\sigma_{22}) - Q_{44}(\sigma_{12}P_1 + \sigma_{23}P_3) + 4a_{11}P_2^3 + 2a_{12}P_2(P_1^2 + P_3^2) + 6a_{111}P_2^5 + 2a_{112}P_2(P_1^4 + 2P_2^2P_1^2 + P_3^4 + 2P_2^2P_3^2) + 2a_{123}P_2P_1^2P_3^2 - g_{11}\frac{\partial^2 P_2}{\partial x_2^2} - g_{44}\left(\frac{\partial^2 P_2}{\partial x_1^2} + \frac{\partial^2 P_2}{\partial x_3^2}\right) = -(F_{11} - F_{44} - F_{12})\frac{\partial \sigma_{22}}{\partial x_2} - F_{12}\frac{\partial}{\partial x_2} Tr\hat{\sigma} + E_2 \quad \text{(C.1b)}$$

$$\Gamma \frac{\partial P_3}{\partial t} + 2P_3(a_1 - Q_{12}(\sigma_{11} + \sigma_{22}) - Q_{11}\sigma_{33}) - Q_{44}(\sigma_{13}P_1 + \sigma_{23}P_2) + 4a_{11}P_3^3 + 2a_{12}P_3(P_1^2 + P_2^2) + 6a_{111}P_3^5 + 2a_{112}P_3(P_1^4 + 2P_3^2P_1^2 + P_2^4 + 2P_2^2P_3^2) + 2a_{123}P_3P_1^2P_2^2 - g_{11}\frac{\partial^2 P_3}{\partial x_3^2} - g_{44}\left(\frac{\partial^2 P_3}{\partial x_1^2} + \frac{\partial^2 P_3}{\partial x_2^2}\right) = -(F_{11} - F_{44} - F_{12})\frac{\partial \sigma_{33}}{\partial x_3} - F_{12}\frac{\partial}{\partial x_3} Tr\hat{\sigma} + E_3 \quad \text{(C.1c)}$$

The derivation is straightforward: $-F_{11}\frac{\partial \sigma_{33}}{\partial x_3} - F_{12}\left(\frac{\partial \sigma_{11}}{\partial x_3} + \frac{\partial \sigma_{22}}{\partial x_3}\right) - F_{44}\left(\frac{\partial \sigma_{13}}{\partial x_1} + \frac{\partial \sigma_{23}}{\partial x_2}\right) = -(F_{11} - F_{44})\frac{\partial \sigma_{33}}{\partial x_3} - F_{12}\left(\frac{\partial \sigma_{11}}{\partial x_3} + \frac{\partial \sigma_{22}}{\partial x_3}\right) = -(F_{11} - F_{44} - F_{12})\frac{\partial \sigma_{33}}{\partial x_3} - F_{12}\frac{\partial}{\partial x_3} Tr\hat{\sigma}$, where $Tr\hat{\sigma} = \sigma_{11} + \sigma_{22} + \sigma_{33}$ and $\frac{\partial \sigma_{13}}{\partial x_1} + \frac{\partial \sigma_{23}}{\partial x_2} \equiv -\frac{\partial \sigma_{33}}{\partial x_3}$.

Elastic stresses existing in the system can be found from Eq.(A.6) as:

$$\sigma_{11} = c_{11}u_{11} + c_{12}(u_{22} + u_{33}) - q_{11}P_1^2 - q_{12}(P_2^2 + P_3^2) - f_{11}\frac{\partial P_1}{\partial x_1} - f_{12}\left(\frac{\partial P_2}{\partial x_2} + \frac{\partial P_3}{\partial x_3}\right), \quad \text{(C.2a)}$$

$$\sigma_{22} = c_{11}u_{22} + c_{12}(u_{11} + u_{33}) - q_{11}P_2^2 - q_{12}(P_1^2 + P_3^2) - f_{11}\frac{\partial P_2}{\partial x_2} - f_{12}\left(\frac{\partial P_1}{\partial x_1} + \frac{\partial P_3}{\partial x_3}\right), \quad \text{(C.2b)}$$

$$\sigma_{33} = c_{11}u_{33} + c_{12}(u_{11} + u_{22}) - q_{11}P_3^2 - q_{12}(P_2^2 + P_1^2) - f_{11}\frac{\partial P_3}{\partial x_3} - f_{12}\left(\frac{\partial P_1}{\partial x_1} + \frac{\partial P_2}{\partial x_2}\right) \quad \text{(C.2c)}$$

$$\sigma_{12} = c_{44}u_{12} - q_{44}P_1P_2 - f_{44}\left(\frac{\partial P_1}{\partial x_2} + \frac{\partial P_2}{\partial x_1}\right), \tag{C.2d}$$

$$\sigma_{13} = c_{44}u_{13} - q_{44}P_1P_3 - f_{44}\left(\frac{\partial P_1}{\partial x_3} + \frac{\partial P_3}{\partial x_1}\right), \tag{C.2e}$$

$$\sigma_{23} = c_{44}u_{23} - q_{44}P_3P_2 - f_{44}\left(\frac{\partial P_2}{\partial x_3} + \frac{\partial P_3}{\partial x_2}\right). \tag{C.2f}$$

Here $q_{44} = \frac{Q_{44}}{s_{44}}$, $c_{44} = \frac{1}{s_{44}}$ and $f_{44} = \frac{F_{44}}{s_{44}}$.

In the virtual absence of a depolarization field, which is true with high accuracy for a vortex type polarization, the divergence $div\vec{P} = \frac{\partial P_i}{\partial x_i}$ should be very small. Indeed, the approximation $div\vec{P} \approx 0$ is valid inside the cylindrical core (see **Fig. S6b**).

We also note the polarization magnitude $P = \sqrt{P_1^2 + P_2^2 + P_3^2}$ is very close to the constant value everywhere, except for the vortex core (see **Fig. S1, middle row**), and its derivative $\frac{\partial P}{\partial \mathrm{x}_3}$ is negligibly small everywhere, except in the immediate vicinity of the vortex core when in contact with the cylinder ends. For this case we obtain that:

$$\frac{\partial Tr\hat{\sigma}}{\partial \mathrm{x}_3} = \frac{\partial}{\partial \mathrm{x}_3}\left[(c_{11} + 2c_{12})Tr\hat{u} - (q_{11} + 2q_{12})P^2 - (f_{11} + 2f_{12})div\vec{P}\right] \approx (c_{11} + 2c_{12})\frac{\partial Tr\hat{u}}{\partial \mathrm{x}_3} \tag{C.3a}$$

and

$$\frac{\partial \sigma_{33}}{\partial \mathrm{x}_3} = \frac{\partial}{\partial \mathrm{x}_3}\left[c_{11}u_{33} + c_{12}(u_{11} + u_{22}) + (q_{11} - q_{12})P_3^2 - q_{12}P^2 - (f_{11} - f_{12})\frac{\partial P_3}{\partial x_3} - f_{12}div\vec{P}\right] \approx$$
$$\frac{\partial}{\partial \mathrm{x}_3}\left[(c_{11} - c_{12})u_{33} + c_{12}\mathrm{Tr}\hat{u} + (q_{11} - q_{12})P_3^2\right] - (f_{11} - f_{12})\frac{\partial^2 P_3}{\partial x_3^2} \tag{C.3b}$$

Assuming that $\frac{\partial Tr\hat{u}}{\partial \mathrm{x}_3} \approx 0$ and using the smallness of P_3, we can obtain the approximate linearized equation for P_3:

$$2a_1^*P_3 - g_{11}^*\frac{\partial^2 P_3}{\partial x_3^2} - g_{44}\left(\frac{\partial^2 P_3}{\partial x_1^2} + \frac{\partial^2 P_3}{\partial x_2^2}\right) \approx Q_{44}(\sigma_{13}P_1 + \sigma_{23}P_2) - (F_{11} - F_{44} - F_{12})(c_{11} - c_{12})\frac{\partial u_{33}}{\partial x_3} + E_3, \tag{C.5}$$

where $a_1^* = a_1 - Q_{12}Tr\hat{\sigma} - (Q_{11} - Q_{12})\sigma_{33} \approx a_1 - Q_{12}(c_{11} + 2c_{12})Tr\hat{u} - (q_{11} + 2q_{12})p^2 - (Q_{11} - Q_{12})[(c_{11} - c_{12})u_{33} + c_{12}\mathrm{Tr}\hat{u}] \approx a_1 - (q_{11} + 2q_{12})p^2 - (Q_{11} - Q_{12})(c_{11} - c_{12})u_{33}$ and $g_{11}^* = g_{11} + (F_{11} - F_{44} - F_{12})(f_{11} - f_{12})$. The simplest 2D polarization vortex can be modeled by the functions

$$P_1 = p(r)sin\varphi,\ P_2 = -p(r)cos\varphi \text{ and } P_3 = 0. \tag{C.6a}$$

These polarization components in cylindrical coordinates are

$$P_r = 0,\ P_\varphi = -p(r) \text{ and } P_3 = 0. \tag{C.6b}$$

It is easy to check that in the case $div\vec{P} = 0$ for arbitrary $p(\rho)$. For a 2D-vortex with an empty core we can assume that $p(\rho) \approx tanh\left(\frac{\rho}{L_C^x}\right)$, where L_C^x is a transverse correlation length.

Using Eqs.(C.6) as a zero approximation we obtain from Eq.(C.2) that $\sigma_{13} = c_{44}u_{13}$, $\sigma_{23} = c_{44}u_{23}$ and $\sigma_{33} = (c_{11} - c_{12})u_{33} + c_{12}\mathrm{Tr}\hat{u} - q_{12}p^2$

$$P_3 \approx \frac{Q_{44}c_{44}p(u_{13}sin\varphi - u_{23}cos\varphi) - (F_{11} - F_{44} - F_{12})(c_{11} - c_{12})\frac{\partial u_{33}}{\partial x_3}}{2\left[a_1 - (q_{11} + 2q_{12})p^2 - (Q_{11} - Q_{12})(c_{11} - c_{12})u_{33} + \left(g_{11} + (F_{11} - F_{44} - F_{12})(f_{11} - f_{12})\right)L_C^z + g_{44}L_C^x\right]}, \tag{C.7a}$$

Next, we consider several model cases. The first case is an absolutely rigid shell covering the ferroelectric core, when the maximal stresses evolved in the system can be roughly estimated from Eqs.(A.8) at $u_{ij} = 0$. The second case corresponds to a very soft shell covering the rigid ferroelectric core, when the stresses are minimal and the strains (at least near the cylinder ends) can be roughly estimated from Eqs.(C.2) at $\sigma_{ij} = 0$. Furthermore, the compatibility conditions should be valid.

Using the relations $q_{11} - q_{12} = (Q_{11} - Q_{12})(c_{11} - c_{12}) = \frac{Q_{11} - Q_{12}}{s_{11} - s_{12}}$, $q_{11} + 2q_{12} = (Q_{11} + 2Q_{12})(c_{11} + 2c_{12}) = \frac{Q_{11} + 2Q_{12}}{s_{11} + 2s_{12}}$, $c_{11} - c_{12} = \frac{1}{s_{11} - s_{12}}$, $c_{44} = \frac{1}{s_{44}}$ and $f_{11} - f_{12} = (F_{11} - F_{12})(c_{11} - c_{12}) = \frac{F_{11} - F_{12}}{s_{11} - s_{12}}$, we obtain that

$$P_3 \approx \frac{\frac{Q_{44}}{s_{44}}p(u_{13}sin\varphi - u_{23}cos\varphi) - \frac{F_{11} - F_{44} - F_{12}}{s_{11} - s_{12}}\frac{\partial}{\partial \mathrm{z}}u_{33}}{2\left[a_1 - \frac{Q_{11} + 2Q_{12}}{s_{11} + 2s_{12}}p^2 - \frac{Q_{11} - Q_{12}}{s_{11} - s_{12}}u_{33} + \left[g_{11} + (F_{11} - F_{44} - F_{12})\frac{F_{11} - F_{12}}{s_{11} - s_{12}}\right]L_C^z + g_{44}L_C^x\right]}, \tag{C.7b}$$

where $\{\rho, \varphi, z\}$ are cylindrical coordinates, the function $p(\rho) \approx tanh\left(\frac{\rho}{L_C^x}\right)$, and L_C^x and are lateral and axial correlation lengths. The functions $u_{ij}(\rho, \varphi, z)$ are elastic strains, s_{ij} are elastic compliances, Q_{ij} are electrostriction tensor components, g_{ij} are polarization gradient coefficients written in Voight notations. From Eq.(C.7bb) the axial part of the flexon polarization is proportional to $-\frac{F_{11} - F_{44} - F_{12}}{s_{11} - s_{12}}\frac{\partial}{\partial \mathrm{z}}u_{33}(\rho, \varphi, z)$, and this proportionality along with **Fig. S6o** qualitatively describes the curves' behavior in **Fig. 3f** and **4f** in the main text**.**

Using Eqs.(C.1), we can "recover" an analog of Eq.(A.2) for a "full" Lifshitz invariant:

$$G_{flexo} = \frac{F_{11} - F_{44} - F_{12}}{2}\left(\sigma_{ii}\frac{\partial P_i}{\partial \mathrm{x}_i} - P_i\frac{\partial \sigma_{ii}}{\partial \mathrm{x}_i}\right) + \frac{F_{12}}{2}\left[Tr(\hat{\sigma})\frac{\partial P_i}{\partial \mathrm{x}_i} - P_i\frac{\partial Tr(\hat{\sigma})}{\partial \mathrm{x}_i}\right], \tag{C.8a}$$

Assuming that $\frac{\partial P_i}{\partial \mathrm{x}_i} \approx 0$ (as it should be for the mostly uncharged domain structures) and making an integration over parts in the second term in Eq.(C.8a), we obtain:

$$G_{flexo} \approx \frac{F_{11}-F_{44}-F_{12}}{2}\left(\sigma_{ii}\frac{\partial P_i}{\partial x_i} - P_i\frac{\partial \sigma_{ii}}{\partial x_i}\right). \qquad \text{(C.8b)}$$

Elementary, but cumbersome calculations lead to an "odd" flexo-field in the boundary conditions $\int_V G_{flexo} \approx \int_V G_0 + \frac{F_{11}-F_{44}-F_{12}}{2}\frac{Q_{11}-Q_{12}}{3}\int_{Si} P_i^3$.

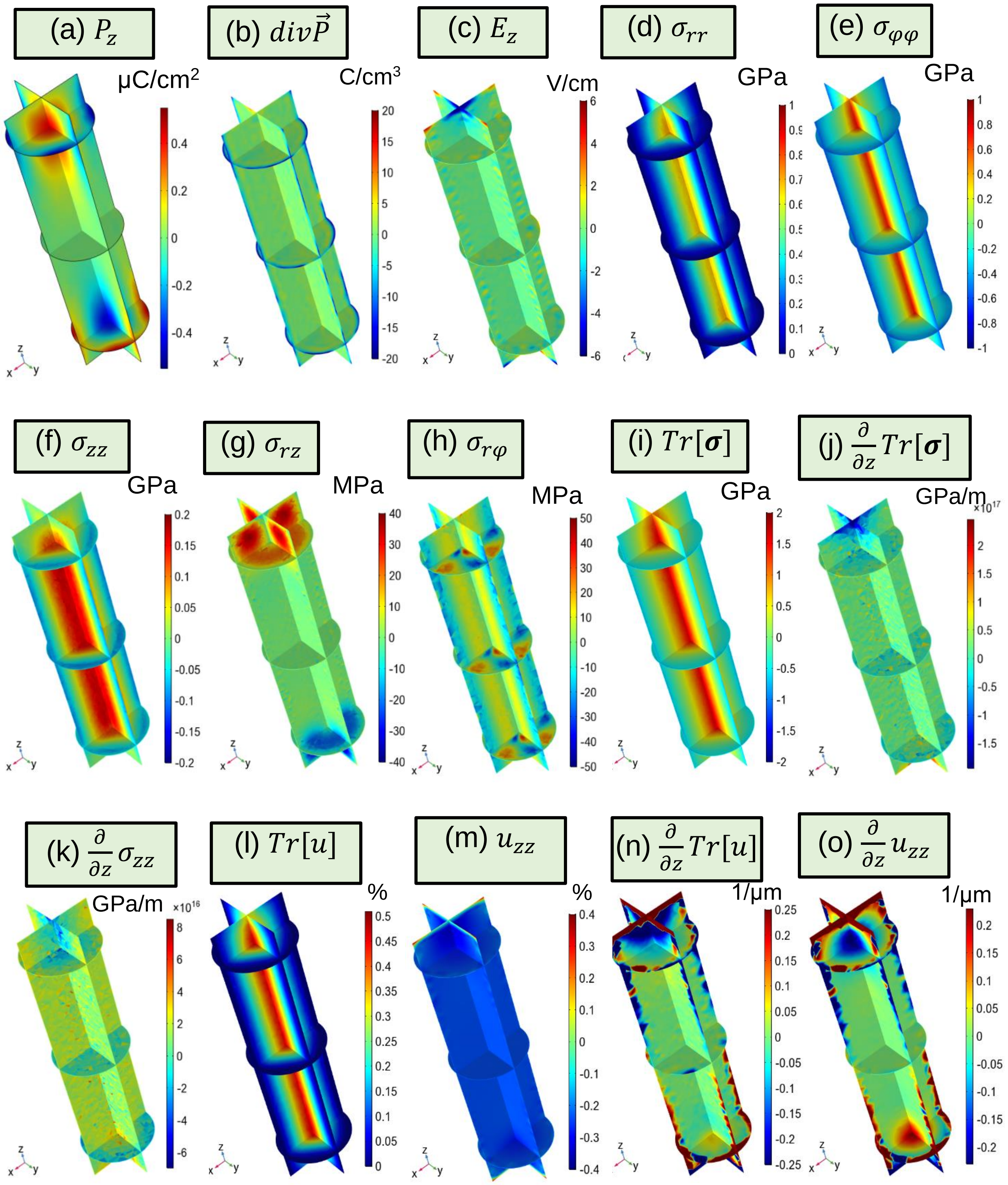

Figure S6. Distribution of polarization component P_z **(a)**, its divergency $div\vec{P}$ **(b)**, electric field component E_z **(c)**, nonzero elastic stresses **(d-i)**, their derivatives **(j, k)**, strain components **(l,m)** and its gradients **(n, o)**

in three different cross-sections of the cylindrical core. A cylindrical coordinate system $\{r, \varphi, z\}$ is used for the mechanical stress, strain, electric field and polarization. Note that the stress component $\sigma_{z\varphi} = 0$ (in spherical coordinates). Temperature $T = 300\ K$. All other parameters are listed in **Table S1**.

Appendix D. Topological Index and Toroidal Moment

First, let us calculate the topological index n of the **unit** polarization orientation [24]

$$n = \frac{1}{4\pi}\int_S \vec{p}\left[\frac{\partial\vec{p}}{\partial x}\times\frac{\partial\vec{p}}{\partial y}\right]dxdy \qquad \text{(D.1)}$$

for zero, positive, and negative flexoelectric tensor coefficients. The integration is performed over the cylinder cross-section, and here $\vec{p} = \frac{\vec{P}}{P}$.

The flexon polarization has the following structure in Cartesian coordinates

$$P_1 \approx p(r,z)\cos[\varphi(\alpha,z)], \quad P_2 \approx p(r,z)\sin[\varphi(\alpha,z)], \quad P_3 \approx \eta(r,z). \qquad \text{(D.2a)}$$

Here $p(r,z) > 0$, and $\varphi(\alpha,z) \approx \alpha - \frac{\pi}{2}$, where α is the polar angle, $x = r\cos\alpha$, and $y = r\sin\alpha$. The polarization magnitude is $P(r,z) = \sqrt{p^2(r,z) + \eta^2(r,z)}$.

Let us introduce the unit polarization as:

$$\vec{p} \approx \{\sin[\theta(r,z)]\cos[\varphi(\alpha,z)],\ \sin[\theta(r,z)]\sin[\varphi(\alpha,z)], \cos[\theta(r,z)]\}, \qquad \text{(D.2b)}$$

where the functions $\sin[\theta(r,z)] = \frac{p(r,z)}{\sqrt{p^2(r,z)+\eta^2(r,z)}}$ and $\cos[\theta(r,z)] = \frac{\eta(r,z)}{\sqrt{p^2(r,z)+\eta^2(r,z)}}$.

The gradients of the unit polarization can be written as

$$\frac{\partial\vec{p}}{\partial x} \approx \left\{\cos[\theta]\cos[\varphi]\frac{\partial\theta}{\partial r}\frac{x}{r} - \sin[\theta]\sin[\varphi]\frac{\partial\varphi}{\partial\alpha}\frac{\partial\alpha}{\partial x},\ \cos[\theta]\sin[\varphi]\frac{\partial\theta}{\partial r}\frac{x}{r} + \right.$$

$$\left. + \sin[\theta]\cos[\varphi]\frac{\partial\varphi}{\partial\alpha}\frac{\partial\alpha}{\partial x}, -\sin[\theta]\ \frac{\partial\theta}{\partial r}\frac{x}{r}\right\}, \qquad \text{(D.2c)}$$

$$\frac{\partial\vec{p}}{\partial y} \approx \left\{\cos[\theta]\cos[\varphi]\frac{\partial\theta}{\partial r}\frac{y}{r} - \sin[\theta]\sin[\varphi]\frac{\partial\varphi}{\partial\alpha}\frac{\partial\alpha}{\partial y},\ \cos[\theta]\sin[\varphi]\frac{\partial\theta}{\partial r}\frac{y}{r} + \right.$$

$$\left. + \sin[\theta]\cos[\varphi]\frac{\partial\varphi}{\partial\alpha}\frac{\partial\alpha}{\partial y}, -\sin[\theta]\ \frac{\partial\theta}{\partial r}\frac{y}{r}\right\}, \qquad \text{(D.2d)}$$

Here we used $\partial r/\partial x = x/r$ and $\partial r/\partial y = y/r$. Below we use the following relations $\frac{y}{r}\cos\alpha = r\sin\alpha\frac{\partial\alpha}{\partial y} \Rightarrow \frac{\partial\alpha}{\partial y} = \frac{x}{r^2}$ and $\frac{\partial r}{\partial x}\sin\alpha + r\ \frac{\partial\alpha}{\partial x}\cos\alpha \Rightarrow \frac{\partial\alpha}{\partial x} = -\frac{y}{r^2}$. After obvious, but tedious transformations we obtain:

$$\vec{p}\left[\frac{\partial\vec{p}}{\partial x}\times\frac{\partial\vec{p}}{\partial y}\right] = \sin[\theta]\frac{\partial\theta}{\partial r}\frac{\partial\varphi}{\partial\alpha}\left(\frac{x}{r}\frac{\partial\alpha}{\partial y} - \frac{y}{r}\frac{\partial\alpha}{\partial x}\right) \equiv \frac{\sin[\theta]}{r}\frac{\partial\theta}{\partial r}\frac{\partial\varphi}{\partial\alpha}. \qquad \text{(D.2e)}$$

Note, that this relation remains unchanged even if one could take into account the radial dependence of polarization magnitude, $P(r,z) = \sqrt{P_1^2 + P_2^2 + P_3^2}$.

Using the representation (D.2b) and reproducing the detailed calculations in Ref. [25], we obtain:

$$n(z) = \int_0^R \sin[\theta(r,z)] \frac{\partial\theta(r,z)}{\partial r} dr \int_0^{2\pi} \frac{\partial\varphi(\alpha,z)}{4\pi\partial\alpha} d\alpha = \frac{1}{4\pi} [\cos[\theta(r,z)]]_{\theta(r=0,z)}^{\theta(r=R,z)} [\varphi(\alpha,z)]_{\alpha=0}^{\alpha=2\pi} \quad \text{(D.3a)}$$

Here R is the cylinder radius. Substituting here $\varphi(\alpha,z) \approx \alpha - \frac{\pi}{2}$ and $\cos[\theta(r,z)] = \frac{\eta(r,z)}{\sqrt{p^2(r,z)+\eta^2(r,z)}}$ we obtain

$$n(z) \approx \frac{1}{2}\left(\frac{\eta(R,z)}{\sqrt{p^2(R,z)+\eta^2(R,z)}} - \frac{\eta(0,z)}{\sqrt{p^2(0,z)+\eta^2(0,z)}}\right) = -\frac{\eta(0,z)}{2\sqrt{p^2(0,z)+\eta^2(0,z)}}, \quad \text{(D.3b)}$$

since $\eta(R,z) = 0$ and $p(R,z) > 0$.

The dependence $n(z)$ is shown in **Fig. S7a** for zero (green horizontal line), positive (3 solid curves), and negative (3 dashed curves) flexoelectric tensor coefficients F_{ij}. The black curves F_{ij} values are listed in **Table S1**; the red curves are calculated for twice the value of F_{ij} (labeled as "$2F_{ij}$") and the blue curves are calculated for six times the value of F_{ij} (labeled as "$6F_{ij}$"). The Z-profile of the axial polarization $P_3(0,z)$ and polarization magnitude $P(0,z)$ are shown in **Fig. S7b** and **Fig. S7c**, respectively. Symbols are calculated by FEM for positive F_{ij} (black diamonds), $2F_{ij}$ (red triangles) and $6F_{ij}$ (blue squires). An applied voltage is absent in **Fig. S7**.

Solid and dashed curves are the interpolation functions.

$$P_3(0,z) = f\frac{z}{L}(1 + Az^2)\left(\tanh\left[\frac{z+\mathrm{z}_m}{\mathrm{z}_0}\right] - \tanh\left[\frac{z-\mathrm{z}_m}{\mathrm{z}_0}\right]\right), \quad \text{(D.4a)}$$

$$P(0,z) = g\frac{1}{L}\sqrt{1+\frac{z^2}{B}}(1 + Az^2)\left(\tanh\left[\frac{z+\mathrm{z}_m}{\mathrm{z}_0}\right] - \tanh\left[\frac{z-\mathrm{z}_m}{\mathrm{z}_0}\right]\right), \quad \text{(D.4b)}$$

$$n(z) = -\frac{\mathrm{f}}{g}\frac{z}{\sqrt{1+(z^2/B)}}. \quad \text{(D.4c)}$$

Here f, g, A, B, z_0, and z_m are the fitting parameters to FEM results, which are listed in **Table S2**. The length scale $L = 1$ nm. The amplitude f increases with the increase of flexoelectric coupling strength and saturates at high $|F_{ij}|$. Since the value $P(0,z)$ is very close to the $P_3(0,z)$ near the cylinder end, but $P_3(0,z)$ vanishes in the nanoparticle center, the topological index continuously changes from -½ to +½ with a z-coordinate change from one cylinder end ($z = -20$ nm) to another ($z = +20$ nm).

Table S2. Fitting parameters for Eqs.(D.4)

Fitting parameter		Flexoelectric coefficients F_{ij}					
	$-6F_{ij}$	$-2F_{ij}$	$-F_{ij}$	0	F_{ij}	$2F_{ij}$	$6F_{ij}$
f (μC/cm^2)	–0.011	–0.0071	–0.0045	0	0.0045	0.0071	0.011
g (μC/cm^2)	0.0305	0.0224	0.0174	N/A	0.0174	0.0224	0.0305
A (nm^{-2})	0.0100	0.0125	0.0110	N/A	0.0110	0.0125	0.0100
B (nm^2)	5	10	15	N/A	15	10	5

z_0 (nm)	1.8	2.2	2.3	N/A	2.3	2.2	1.8
z_m (nm)	17.8	17.5	17.5	N/A	17.5	17.5	17.8

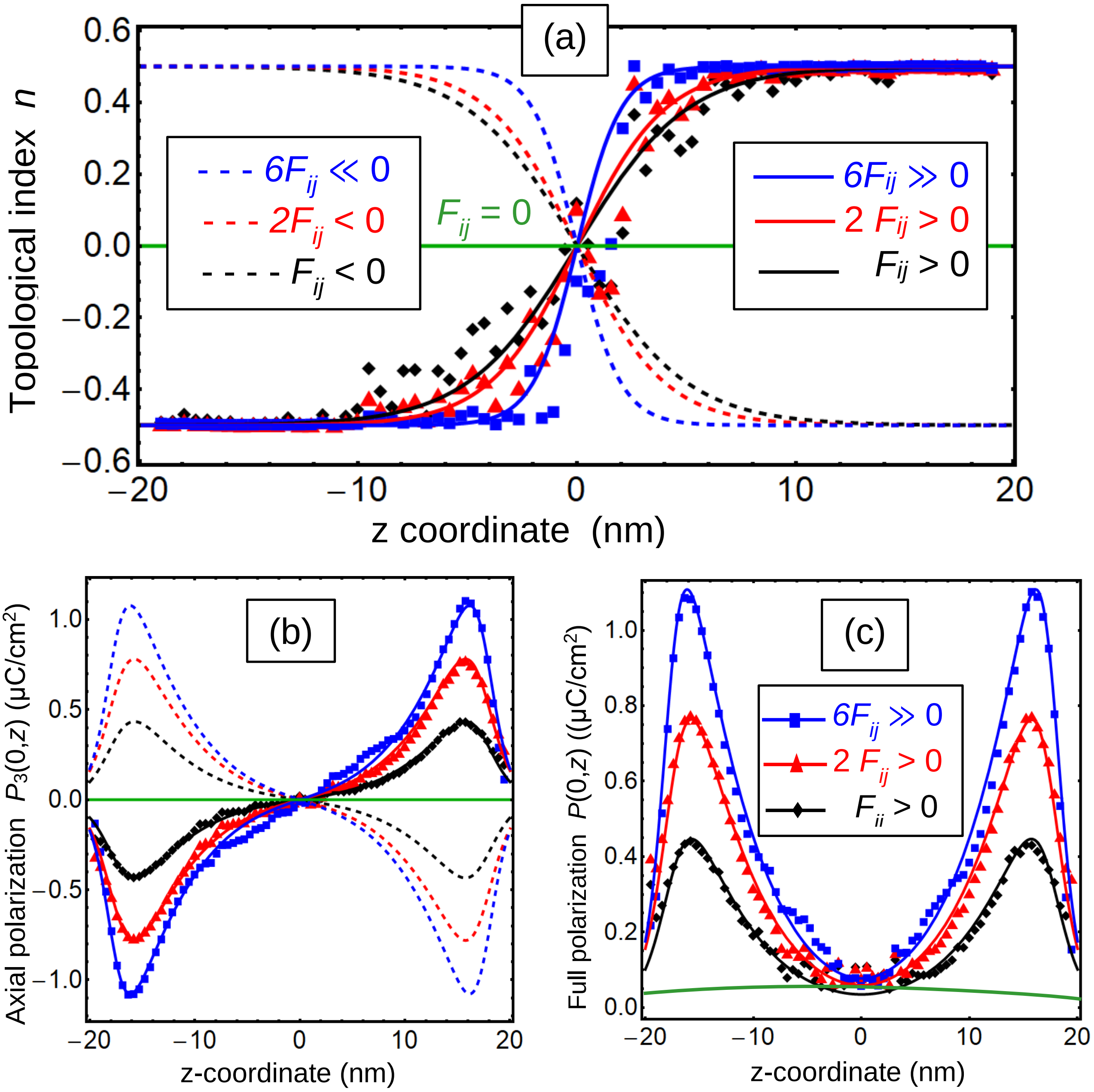

Figure S7. **(a)** Z-dependence of the polarization orientation topological index $n(z)$ for zero (green horizontal line), positive (solid curves), and negative (dashed curves) flexoelectric tensor coefficients F_{ij}. For the black curves F_{ij} values are listed in **Table S1**, for the red curves we used $2F_{ij}$, and blue curves, we used $6F_{ij}$. **(b-c)** Z-profile of the axial polarization P_3 **(b)** and polarization magnitude P **(c)** calculated at $r = 0$. Symbols are calculated by FEM for positive F_{ij} (black diamonds), $2F_{ij}$ (red triangles), and $6F_{ij}$ (blue squires). Solid and dashed curves are fitting functions listed in the text. Referenced values of F_{ij} and all other parameters are given in **Table S1.** Temperature $T = 300\ K$, $U = 0$.

As a next step, let us calculate the toroidal moment (**TM**):

$$\vec{M} = \frac{1}{V}\int_V [\vec{P} \times \vec{r}]\, d^3 r \qquad \text{(D.5)}$$

The integration here is performed over the nanoparticle volume $V = \pi R^2 h$. The toroidal moment (D.5) is independent on the coordinate origin of radius-vector $\vec{r}$, only if all three components of electric polarization have a zero average over the nanoparticle volume. This is true in the considered case for $U = 0$ (no applied voltage).

Let us estimate the toroidal moment using the following approximation for polarization distribution:

$$P_1 \approx p(r,z)\sin[\alpha], \quad P_2 \approx -p(r,z)\cos[\alpha], \quad P_3 \approx \eta(r,z), \qquad \text{(D.6a)}$$

where the coordinates are

$$x = r\cos[\alpha], \qquad y = r\sin[\alpha], \qquad z = z. \qquad \text{(D.6a)}$$

The vectorial product is:

$$[\vec{P} \times \vec{r}] = -\overrightarrow{e_x}(p(r,z)\cos[\alpha]\, z + \eta(r,z) r \sin[\alpha]) + \overrightarrow{e_y}(\eta(r,z) r \cos[\alpha] - p(r,z)\sin[\alpha]\, z) + \overrightarrow{e_z} p(r,z) r \qquad \text{(D.7a)}$$

After the integration we obtain that only the z-component of the TM is nonzero:

$$\vec{M} \approx \overrightarrow{e_z}\frac{2}{R^2}\int_0^R p(r,z) r\, dr. \qquad \text{(D.7b)}$$

Since the magnitude $p(r,z)$ is almost independent of the flexoelectric coupling (see e.g. **Fig. S4,** the middle row), the TM appears nearly the same for zero, positive, and negative flexoelectric tensor coefficients. To make an analytical estimate in Eq.(D.7b), one can use the following approximation for the magnitude $p(r,z) \cong p_0 tanh\left(\frac{r}{r_0}\right)$, where the p_0 and r_0 are temperature-dependent. This results in:

$$\vec{M} \approx \overrightarrow{e_z} p_0 \left\{1 - d^2\left(\frac{\pi^2}{12} + \mathrm{PolyLog}\left[2, -e^{-\frac{2}{d}}\right]\right) + 2d\,\mathrm{Log}\left[1 + e^{-\frac{2}{d}}\right]\right\}, \qquad \text{(D.8)}$$

where $d = \frac{r_0}{R}$ and $\mathrm{PolyLog}[x]$ is a polylogarithmic function. **Figure S8** shows the dependence of the normalized TM $\frac{M}{p_0}$ on the parameter *d*.

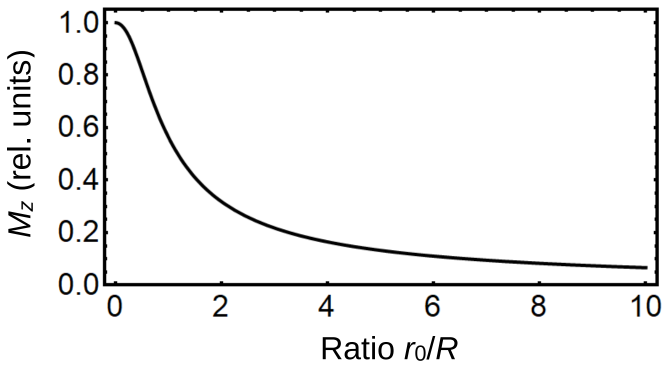

Figure S8. The dependence of the normalized toroidal moment $\frac{M}{p_0}$ on the parameter *d*.

References

---

1 S. Lin, T. Lü, C. Jin, and X. Wang. Size effect on the dielectric properties of $BaTiO_3$ nanoceramics in a modified Ginsburg-Landau-Devonshire thermodynamic theory. Phys. Rev. B **74**, 134115 (2006).

2 E. A. Eliseev, A. V. Semchenko, Y. M. Fomichov, M. D. Glinchuk, V. V. Sidsky, V. V. Kolos, Yu M. Pleskachevsky, M. V. Silibin, N. V. Morozovsky, and A. N. Morozovska, Surface and finite size effects impact on the phase diagrams, polar, and dielectric properties of (Sr, Bi)Ta_2O_9 ferroelectric nanoparticles, J. Appl. Phys. **119**, 204104 (2016).

3 E. A. Eliseev, Y. M. Fomichov, S. V. Kalinin, Y. M. Vysochanskii, P. Maksymovich and A. N. Morozovska. Labyrinthine domains in ferroelectric nanoparticles: Manifestation of a gradient-induced morphological phase transition. Phys. Rev. B **98**, 054101 (2018).

4 A. N. Morozovska, Y. M. Fomichov, P. Maksymovych, Y. M. Vysochanskii, and E. A. Eliseev. Analytical description of domain morphology and phase diagrams of ferroelectric nanoparticles. Acta Mater. **160**, 109 (2018).

5 A. N. Morozovska, M. D. Glinchuk, E. A. Eliseev. Phase transitions induced by confinement of ferroic nanoparticles. Phys. Rev. B **76**, 014102 (2007).

6 H. Huang, C. Q. Sun, P. Hing. Surface bond contraction and its effect on the nanometric sized lead zirconate titanate. J. Phys.: Condens. Matter **12,** L127 (2000).

7 H. Huang, C. Q. Sun, Z. Tianshu, P. Hing. Grain-size effect on ferroelectric $Pb(Zr_{1-x}Ti_x)O_3$ solid solutions induced by surface bond contraction. Phys. Rev. B **63**, 184112 (2001).

8 W. Ma. Surface tension and Curie temperature in ferroelectric nanowires and nanodots. Appl. Phys. A **96**, 915 (2009).

---

9 J. J. Wang, X. Q. Ma, Q. Li, J. Britson, Long-Qing Chen, Phase transitions and domain structures of ferroelectric nanoparticles: Phase field model incorporating strong elastic and dielectric inhomogeneity, Acta Mater. **61**, 7591 (2013).

10 J. J. Wang, E. A. Eliseev, X. Q. Ma, P. P. Wu, A. N. Morozovska, and L.-Q. Chen. Strain effect on phase transitions of $BaTiO_3$ nanowires. Acta Mater. **59**, 7189 (2011).

11 E. A. Eliseev, Y. M. Fomichov, S. V. Kalinin, Y. M. Vysochanskii, P. Maksymovich and A. N. Morozovska. Labyrinthine domains in ferroelectric nanoparticles: Manifestation of a gradient-induced morphological phase transition. Phys. Rev. B **98**, 054101 (2018).

12 J. J. Wang, E. A. Eliseev, X. Q. Ma, P. P. Wu, A. N. Morozovska, and Long-Qing Chen. Strain effect on phase transitions of $BaTiO_3$ nanowires. Acta Materialia **59**, 7189 (2011).

13 A. N. Morozovska, E. A. Eliseev, Y. A. Genenko, I. S. Vorotiahin, M. V. Silibin, Ye Cao, Y. Kim, M. D. Glinchuk, and S. V. Kalinin. Flexocoupling impact on the size effects of piezo- response and conductance in mixed-type ferroelectrics-semiconductors under applied pressure. Phys. Rev. B **94,** 174101 (2016).

14 L. D. Landau, and I. M. Khalatnikov. On the anomalous absorption of sound near a second order phase transition point. In Dokl. Akad. Nauk SSSR, **96**, 469 (1954).

15 J. Hlinka, Mobility of Ferroelectric Domain Walls in Barium Titanate, Ferroelectrics **349,** 49 (2007).

16 J. Hlinka and P. Márton, Phenomenological model of 90-degree domain wall in BaTiO3 type ferroelectrics. Phys. Rev. B **74**, 104104 (2006).

17. E. A. Eliseev, Y. M. Fomichov, S. V. Kalinin, Y. M. Vysochanskii, P. Maksymovich and A. N. Morozovska. Labyrinthine domains in ferroelectric nanoparticles: Manifestation of a gradient-induced morphological phase transition. Phys. Rev. **B 98**, 054101 (2018).

18. A. N. Morozovska, Y. M. Fomichov, P. Maksymovych, Y. M. Vysochanskii, and E. A. Eliseev. Analytical description of domain morphology and phase diagrams of ferroelectric nanoparticles. Acta Materialia **160**, (2018) 109

19 A. K. Tagantsev, G. Gerra, and N. Setter, Short-range and long-range contributions to the size effect in metal-ferroelectric-metal heterostructures. Phys. Rev. **B 77**, 174111 (2008).

20 M. Stengel and N. A. Spaldin, Origin of the dielectric dead layer in nanoscale capacitors, Nature (London) **443,** 679 (2006).

21 M. Stengel, D. Vanderbilt, and N. A. Spaldin, First-principles modeling of ferroelectric capacitors via constrained displacement field calculations, Phys. Rev. B **80,** 224110 (2009).

---

22 S.P. Timoshenko, J.N. Goodier, Theory of Elasticity, McGraw-Hill, N. Y., 1970.

23 I. Ponomareva, A.K. Tagantsev, L. Bellaiche, Finite-temperature flexoelectricity in ferroelectric thin films from first principles, Phys. Rev. B **85**, 104101 (2012).

24 K. Everschor-Sitte, J. Masell, R. M. Reeve, and M. Kläui. Perspective: Magnetic skyrmions—Overview of recent progress in an active research field. J. Appl. Phys. **124**, 240901 (2018).

25 https://physics.stackexchange.com/questions/587236/skyrmion-number